Geochronological and Structural insights into the evolution of the Lower Burra and Callana Groups near Arkaroola: Structural mapping and U-Pb metamorphic monazite dating.

Thesis submitted in accordance with the requirements of the University of Adelaide for an Honours Degree in Geology

William J. Morphett
November 2013

THE UNIVERSITY
of ADELAIDE

LOWER ADELADIAN: STRUCTURE AND METAMORPHISM

ABSTRACT

The lowermost sediments of the Adelaide Supergroup near Arkaroola display pronounced structural complexity and anomalously high metamorphic grade. The timing of the structures, fabrics and metamorphism in the region remain unconstrained, although all are currently interpreted to have occurred during the Delamerian Orogeny. Monazite U/Pb geochronology provides a useful technique for dating amphibolites facies rocks and, combined with map scale and micro structural observations, suggests the peak metamorphism and at least one deformation event occurred significantly earlier than the Delamerian Orogeny. Monazite derived ^{206}Pb/^{238}U age estimates place the timing of peak metamorphism at 705.2±7.4 Ma with observations from thin section revealing a bedding parallel fabric pre-dating peak metamorphism. U/Pb analysis also reveals a second monazite growth event at 644.2±8 Ma the cause of which is hypothesised to be fluid related. Regional folding and axial planar fabric generation post-dates this metamorphism and can be seen to overprint the earlier fabric and wrap the cordierite porphyroblasts. This final deformation event remains largely unconstrained as in situ dating of monazite was not possible in this study. The inferred parasitic relationship between the folds within the studied region and the Arkaroola Syncline which folds the youngest sediments in the Adelaidian Sequence allows for the deposition to be constrained subsequent to the conclusion of the Adelaide Rift Complex.

KEYWORDS

Geochronology, structural geology, Burra Group, Callana Group, metamorphism, monazite, LA-ICP-MS, amphibolites, Arkaroola, Paralana.

LOWER ADELADIAN: STRUCTURE AND METAMORPHISM

Contents

LOWER ADELADIAN: STRUCTURE AND METAMORPHISM

LIST OF FIGURES AND TABLES

Figure 8: Both a and b show a corderite porphyroblast under cross-polarised light situated in a thin section cut from sample R-15. A shows the relationship between

LOWER ADELADIAN: STRUCTURE AND METAMORPHISM

INTRODUCTION

The Arkaroola region of the northern Flinders Ranges is a region of anomalous structural complex and high metamorphic grade compared to other areas of the Adelaide fold belt (Mildren & Sandiford 1995, Sandiford *et al.* 1998a, Sandiford *et al.* 1998b, McLaren *et al.* 2002). It is one of the few areas to expose the lowermost units of the Adelaidean Sedimentary Package (the Callana and lower Burra Groups) and provides an opportunity to study the earliest tectonic history of the "Adelaide Geosyncline"(Preiss 2000). Despite this, there is little geochronological data constraining the timing of metamorphism and deformation in the region. A temporal link between deformation and metamorphism is often assumed, sometimes leading to the timing of metamorphism being incorrectly interpreted. This may be the case for attribution of peak metamorphism and deformation in the Arkaroola region to the Delamerian Orogen (Mildren & Sandiford 1995, Sandiford *et al.* 1998a, Paul *et al.* 1999), despite the fact that geochronological constrains for the Delamerian Orogney are derrived from more than 600 km to the south in the Adelaide Fold Belt (Foden *et al.* 2006). In the Northern Flinders Ranges, the nature of the regional folding is such that it would more likely be related to exhumation and cooling rather than burial and deformation. A model of radiogenic metamorphism (Mildren & Sandiford 1995, Sandiford *et al.* 1998a) would not have to be coupled to deformation and would be more likely related to burial and the generation of a anomalously high geothermal gradient. This suggests the possibility of metamorphism prior to the deformation. There is also the possibility of prolonged metamorphism which may be linked to epithermal activity in the region post-Delamerian. This is of course, assuming all deformation in the region occurred during the Delamerian which may not be the case. Hence tighter geo-chronological constraints

are required to resolve the timing of metamorphism and structure formation within the region.

Whilst there has been much study of the Mount Painter Inlier (Elburg *et al.* 2001, Brugger *et al.* 2003, Elburg *et al.* 2003, Brugger *et al.* 2005, Bakker & Elburg 2006, Brugger *et al.* 2011, Weisheit *et al.* 2013), there has been little detailed research on the metamorphism and structure of the lower Burra and Callana sedimentary packages. Previous honours students (Hansberry 2011, Job 2011) have identified complex structural features in the Arkaroola region that are indicative of several overprinting deformation events.

A number of previous researchers (Mildren & Sandiford 1995, Sandiford *et al.* 1998a) have developed a metamorphic model whereby radiogenic heat production and insulative effect of overlying sediments led to the pressure and temperature (PT) conditions required for the observed metamorphic grade, up to mid-amphibolite facies assumed to have occurred during the Delamerian Orogeny (c. 515-495 Ma) (Foden *et al.* 2006). Some research has been conducted on the cooling pathways experienced by the region, indicating that the region experienced quite a complicated retrograde temperature pathway with several periods of re-heating. Furthermore, it is evident that while the folding events initiated during the Delamerian, they continued through the whole Palaeozoic (McLaren *et al.* 2002).

In this paper we use structural mapping and microstructural analysis in combination with U-Pb dating of metamorphic monazite grians in order to determine the age of the earliest metamorphic event, and structural evolution of the Arkaroola region. The use of monazite as a metamorphic geochronomitor for amphibolite facies conditions has long been recognised. This is due to its affinity to U, resistance to Pb

LOWER ADELADIAN: STRUCTURE AND METAMORPHISM

diffusion and correspondingly high inferred closure temperature (750 C) (Parrish 1990) and its tendency to form as a metamorphic phase at amphibolites facies PT conditions (Parrish 1990, Foster *et al.* 2002). This, coupled with the propensity for monazite to partition into discrete age domains during metamorphic and epithermal fluid alteration (Gibson *et al.* 2004, Martins *et al.* 2009, Williams *et al.* 2011), will allow for tighter age constraints to be placed on the metamorphic history of the lower Adeladian sequences at Arkaroola.
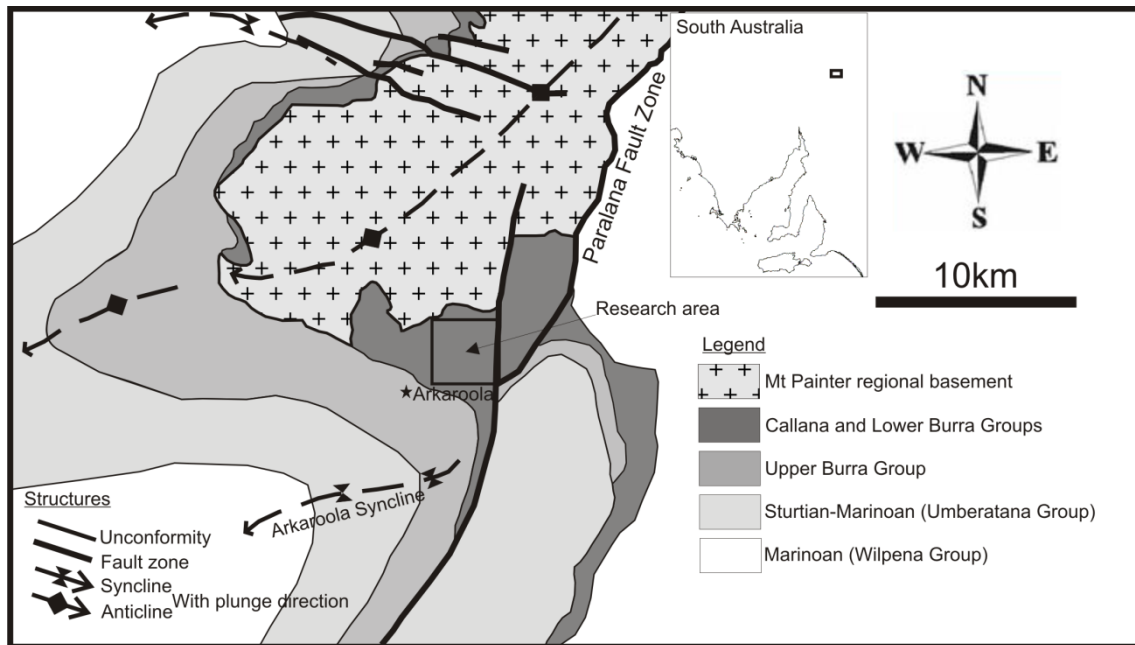
Figure 1: Regional geological map of the Arkaroola region showing major tectonic structures and general lithological boundaries. The insert shows the location of the region in South Australia.

GEOLOGICAL SETTING

Arkaroola is located in the Northern Flinders Ranges, approximately 650 kilometres north of Adelaide (Figure 1). This study is focussed on the lower Adelaidean stratigraphy inclusive of the Callanna beds within the Arkaroola sub group and the lower Burra Group within the Emeroo Sub Group(Gibson *et al.* 2004) which are exposed immediately to the north of the Arkaroola Village. Geologically, the project

LOWER ADELADIAN: STRUCTURE AND METAMORPHISM

area is located in the tectonic subdivision of the Adelaide Rift Complex known as the Northern Flinders Ranges (Drexel *et al.* 1993, Preiss 2000).

The Adelaidean metasedimentary sequences overlie and dip outward from an anticlinal core of highly metamorphosed Paleo- to Mesoproterozoic basement rocks of the Mount Painter Inlier (Mildren & Sandiford 1995, Brugger *et al.* 2005, McLaren *et al.* 2006). The Mt. Painter Inlier consists of metasedimentary and meta-igneous rocks that were deposited and underwent at least one period of deformation and metamorphism during the early Mesoproterozoic. The meta-igneous rocks are predominantly radioactive, high heat producing granites (Sandiford *et al.* 1998a, Elburg *et al.* 2003, Brugger *et al.* 2005, Brugger *et al.* 2011, Elburg *et al.* 2013).

The deposition of the Callanna beds commenced with the unconformable deposition of the massive, quartzite unit, the Paralana Quartzite, above Paleo to Mesoproterozoic rocks of the Mt. Painter Inlier. The Paralana Quartzite is thought to have been deposited at onset of NW-SE extension at least 830 Ma (Powell *et al.* 1994) but more likely is as old as 840 Ma to account for sedimentary thickness (Preiss 2000). The Paralana Quartzite was conformably overlain by the Wywyana Formation, a mixture of clastics, evaporates and carbonates, and subsequently by the Wooltana Volcanics, with an inferred depositional age of 827 ± 6 Ma(Drexel *et al.* 1993). The Wooltana Volcanics consist of a sequence of basalts, rhyolites and volcaniclastics which inconsistently overlie and are inter-fingered by the Wywyana Formation(Paul *et al.* 1999, Preiss 2000). In the studied area, The Wooltana Volcanics are disconformably overlain by metasedimentary rocks of the lower Burra Group(Drexel *et al.* 1993).

Deposition of Burra Group began at approximately 780 Ma (Drexel *et al.* 1993) with the deposition of the Humanity Seat Formation, comprised of heavy mineral

LOWER ADELADIAN: STRUCTURE AND METAMORPHISM

laminated quartzite and conglomerates, locally above the Wooltana Volcanics. This occurred around 50 million years after the eruption of the Wooltana Volcanics and hence the uncomformal boundary (Preiss 2000, Gibson *et al.* 2004). Stratigraphically above lies the Woodnamooka "Phyllite", consisting of silt an sandstones, which itself is overlain by the Blue Mine Conglomerate (Drexel *et al.* 1993, Mildren & Sandiford 1995, Preiss 2000). We are uncomfortable using a metamorphic textural term for a name of a package of sediments that have been subject to various degrees of metamorphism and alteration. Therefore this package will be henceforth referred to as the "Woodnamooka Formation" this paper.

There is at this point, a fairly abrupt change from a relatively low energy deposition environment with a likely comparatively distant sedimentary source, to a very near-source sedimentary environment, with the source most likely being granitic due to the abundance of angular potassium feldspar clasts. The likely cause of this is currently poorly understood and is not mentioned in any literature and hence warrants investigation. Subsequent to this there were at least two more rifting events interspersed with sag phases, allowing for the deposition of the remainder of the Adelaidean sedimentary package (Drexel *et al.* 1993, Preiss 2000).

Deformation and, predominantly low-grade, metamorphism in the Adelaide Fold Belt has previously been attributed to the Delamerian Orogeny (Mildren & Sandiford 1995, Sandiford *et al.* 1998a, Preiss 2000, Foden *et al.* 2006, McLaren *et al.* 2006). Dating of variably deformed intrusive phases from the southern Adelaide Fold Belt has constrained the Delamerian Orogeny to between 515 ± 2 Ma and 492 ± 2 Ma (Foden *et al.* 2006). This is widely assumed to be the time in which peak metamorphic temperatures of amphibolites facies were reached within the Callanna and lower Burra

LOWER ADELADIAN: STRUCTURE AND METAMORPHISM

Groups in the Arkaroola region, resulting in the growth of muscovite, biotite, and discrete cordierite zones within the Woodnamooka Formation. However there are no independent geochronological constraints on the timing of peak metamorphism in the Northern Flinders Ranges. This presence of cordierite indicates pressures never exceeded that of burial greater than 10 km(Mildren & Sandiford 1995).

Subsequent to the Delamerian Orogeny, there is evidence to suggest that the Arkaroola Subgroup and the Emeroo Subgroup underwent a prolonged cooling with one article presenting some evidence for three separate periods of cooling with the first beginning subsequent to the Delamerian Orogeny, the seccond at 430 to 400 Ma, and the third at 330 to 325 Ma (McLaren *et al.* 2002). The increased temperature period between 400 and 330 Ma is interesting as it suggests possible influences from the long-lived, Alice Springs Orgeny due to similarities in timing (440 – 300 Ma according to muscovite $^{40}Ar/^{39}Ar$ dating) (McLaren *et al.* 2009). There is also evidence of major, hydrothermal activity occurring between 460 and 440 Ma, coinciding with the magmatic activity responsible for the intrusion of the British Empire granite (Brugger *et al.* 2005, Elburg *et al.* 2013).

Post Delamerian, the region underwent an extended period of burial until the late Miocene at which time modern tectonic forces generated the uplift which has created the modern day topography. Currently the ranges are still being uplifted at rates of between 20 - 160 m Myr^{-1} (Quigley *et al.* 2007).

LOWER ADELADIAN: STRUCTURE AND METAMORPHISM

METHODS

Mapping

The research area mapped is bound on the southern side by the Arkaroola village road, on the west and north by the Echo Camp backtrack and on the east by north-south trending ridges governed by the Paralana Fault. The total area mapped is approximately 16 square kilometres (Figure 2).

Structural mapping of the research area was conducted through field transects collecting bedding and foliation information and observations on rock types coupled with the use of Quickbird aerial photography of the region at 1:10 000 scale. Lithological boundaries and structural features were inferred from analysis of structural data, field observations, and interpretation of the aerial images. Cross sections were derived from the data represented by the map (Figure 3).

Sample collection and preparation

Fifteen oriented rock samples were taken in the mapping area (figure 2) representing each of the mapped units. Representative exposures where selected based upon weathering, mineralogy and ease of hand specimen removal. Samples of in situ portions of outcrop were removed using a sledge hammer after being photographed and having their dip and dip direction marked and recorded.

Orientated thin sections of these samples were cut perpendicular to foliation for tectonic fabric analysis. The remainder of the sample was crushed using a jaw crusher and disk mill consecutively and the 79µm to 450µm fraction was separated using a sieve. Separated monazites were then obtained using panning, Franz (between 0.6 nT

and 0.7nT) and heavy liquid methods prior to being handpicked and mounted in epoxy resin blocks (Howard *et al.* 2011).

Sample analysis

Thin sections were viewed under transmitted light microscope and SEM, both to look for multiple fabrics and evidence of multiple stages of metamorphism and to determine the plausibility of in-situ dating of monazite. Unfortunately, all monazites located in thin section under the SEM were too small (<10µm) to be of use for in-situ dating through Laser ablation inductively coupled plasma mass spectrometry (LA ICP-MS).

Few of the selected samples contained sufficient monazite for analysis. From these we selected samples R-12 and R-15 for analysis due to their monazite yield and potential to contain monazite of different generations preserved in porphyroblasts. The two samples were taken from widely separated locations within a comparable stratigraphic location (Figure 2). Back scatter electron (BSE) images were obtained using a XL40 scanning electron microscope (SEM) for compositional zoning analysis. Compositional maps of Ce, Pb, Th, U and Y of selected monazite grains were generated using an SX5 Electon Micro probe (EPMA).

LA ICP-MS was selected as the dating method for the separated monazites as it allows for the fast and relatively accurate dating of a large quantity of sample when compared to electron microprobe and SHRIMP techniques (Košler 2007). While not possessed of the accuracy of SHRIMP dating due to the size of the laser spot and error inherent in the ablation of a portion of the sample, the laser ablation method is still possessed of the accuracy required (Paquette & Tiepolo 2007) to constrain the differences in ages that have been hypothesised. U-Pb isotopic analyses where gathered

using a New Wave 213nm Nd-YAG laser in an He ablation atmosphere coupled to an Agilent 7500cs ICP-MS. 30s of gas blank was analysed followed by 60s of analysis during monazite ablation. Prior to ablation, the laser was fired for 10s with the shutter closed to allow for beam stabilization. The beam diameter was approximately 12 µm at sample surface. Isotopes concentrations analysed were ^{204}Pb for 10ms, ^{206}Pb for 15ms, ^{207}Pb for 30ms, and ^{238}U for 15ms.

Ages of monazites were calculated using the real-time correction program 'Glitter' developed at Macquarie University, Sydney (Jackson *et al.* 2004). The correction of the U-Pb fraction was achieved through the use of the MAdel monazite standard (TIMS normalisation data: ^{207}Pb/^{206}Pb=490.7 Ma, ^{206}Pb/^{238}U=514.8 Ma and ^{207}Pb/^{235}U=510.4 Ma). Prior to unknown analysis, corrected age accuracy was confirmed through analysis of an in-house monazite standard with a reported ^{206}Pb/^{238}U age of 450.2 ± 3.4 Ma.

The results attained from LA ICP-MS were analysed in conjunction with the BSE images and the EPMA compositional maps to determine the effect of possible laser spot overlap upon the ages calculated by Glitter. Through this, it was possible to discount data that clearly derived from mixed compositional domains within the monazite crystal. Data was plotted on concordia diagrams, frequency diagrams and weighted averaged diagrams and ages calculated using Isoplot (version3) (Ludwig 2012).
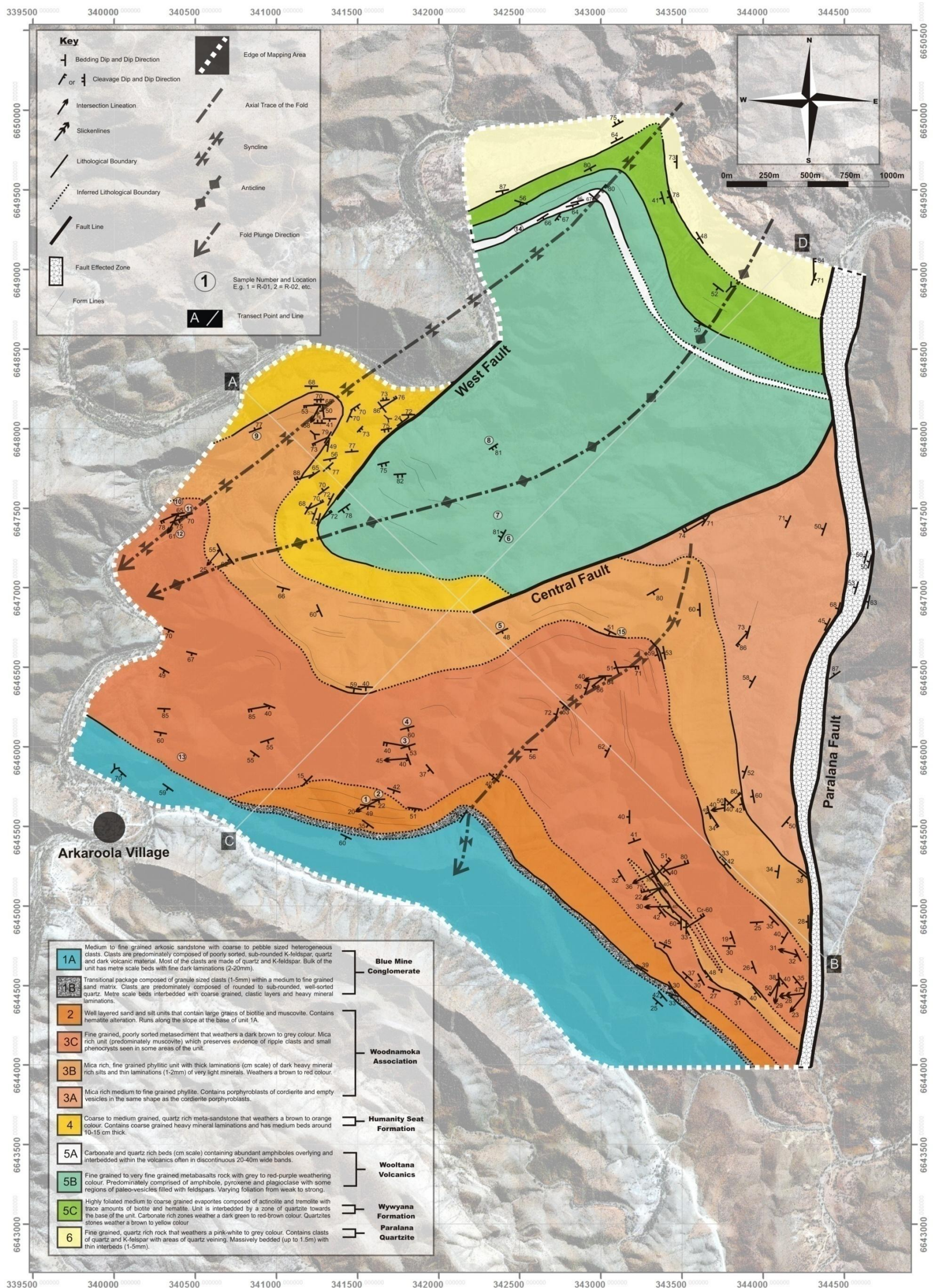
Figure 2: Geological map of the researched region showing major structural features, lithological boundaries, structural readings and sample locations. Cross section transects are shown as white lines between A and B and C and D.

LOWER ADELADIAN: STRUCTURE AND METAMORPHISM

RESULTS

Stratigraphy

We identified 10 lithological units, including transitional packages, of varying

thicknesses (Figure 3) within the research area. These have been grouped under the

following 6 defined rock units arranged from oldest to youngest; the Paralana Quartzite,

The Wooltana Volcanics, the Humanity Seat Formation, the Woodnamooka Formation,

and the Blue Mine Conglomerate (Drexel *et al.* 1993). These do not encompass the

fault altered mixture of lithologies found within the Paralana Fault zone (Figure 2).

PARALANA QUARTZITE

The Paralana Quartize (figure 2) is a quartz dominated sedimentary unit unconformably

overlying the basement. Cross beds preserving younging direction can be observed at

decimetre scale preserved in heavy mineral laminations. Bedding in this unit is meter to

decimetre scale and is often hard to define due to the lack of compositional variance.

The local thickness of this unit in our research area cannot be attained as the contact of

the Paralana Quartzite with the Mt Painter Inlier was not observed.

WYWYANA FORMATION.

The Wywyana Formation is a mineralogically heterogeneous unit consisting of inter-

bedded quartzites, calc-silicate rocks and carbonates that we interpret to be altered

evaporites conformably overlying the Paralana Quartzite. Locally, the quartzite beds are

consistently between 30 centimetres to 1 meter thick and display some cross-bedding

near

LOWER ADELADIAN: STRUCTURE AND METAMORPHISM
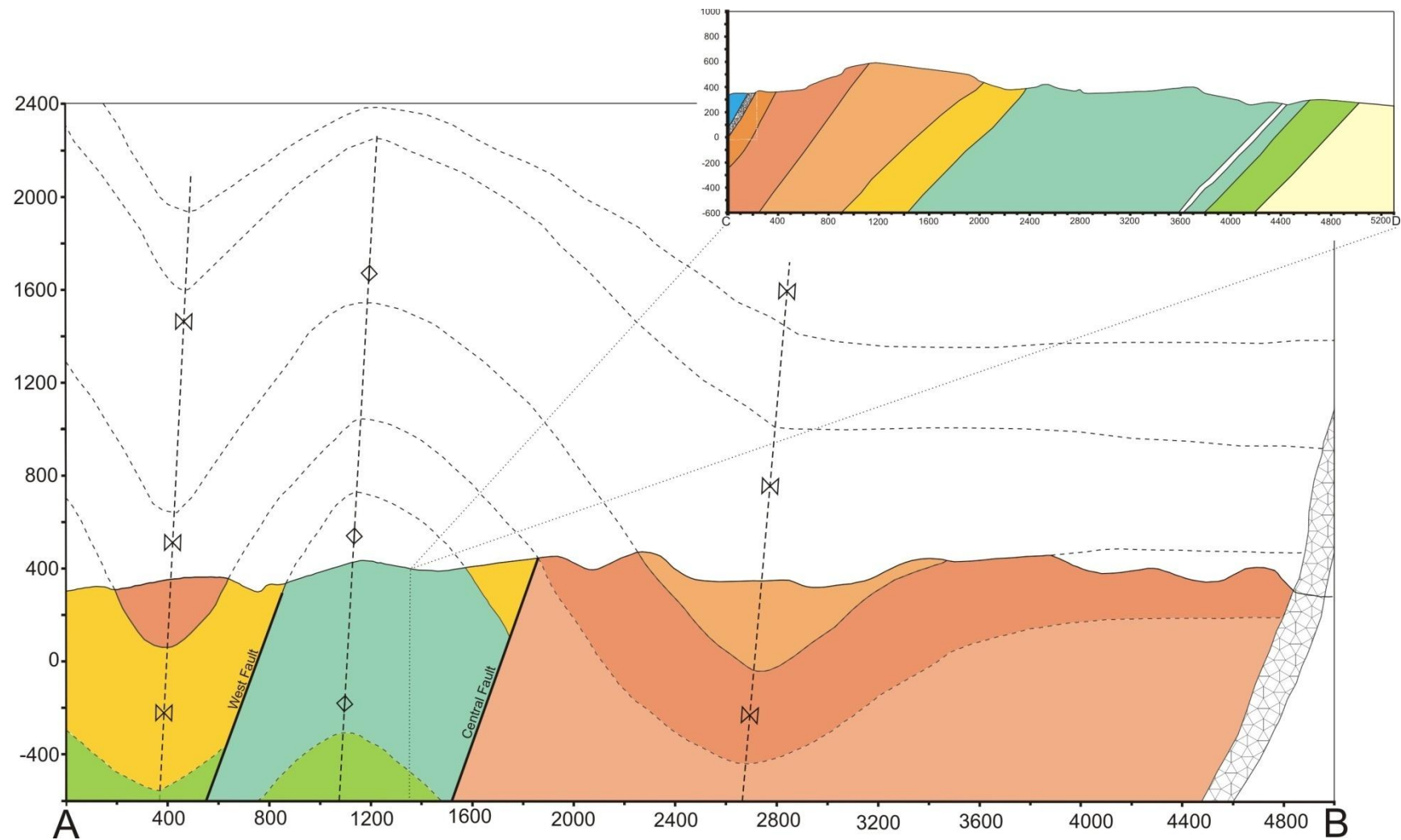
Figure 3: Main image displays a cross section from A to B (seen in figure 2) of the major structural features in the researched area. Insert shows cross section from C to D showing overall lithological thicknesses from the aforementioned points on figure 2. See figure 2 for legend for lithological units.

preserved in heavy mineral laminations. Between these bands of quartzites, are beds of monomineralic, un-orientated actinolite and trace epidote which are 30 to 40 cm in thickness (Figure 4). Large sections of the unit consist of disordered zones of coarse-grained, randomly orientated carbonates, actinolite, tremolite and trace epidote, in which there is no evidence of primary bedding. The thickness of this unit varies but it is generally around 300 meters.

WOOLTANA VOLCANICS

The Wooltana Volcanics consist of metamorphosed basalts and lesser interbedded sedimentary horizons conformably overlying the Wywyana Fromation.

The basalts are deposited in a series of flows 1-7 m thick with vesiculated flow tops and more massive crystalline bases beneath the vesiculated zone. Minerologically, the unit is primarily comprised of amphiboles and micas of varying grain sizes with large crystal growths of unoriented actinolite in some areas. The fossil vesicles describing the tops of the discrete lava flows are now filled with plagioclase.

The metasedimentary component consists of quartz-rich beds containing abundant amphibole and trace epidote similar to the underlying Wywyana Formation with bedding cm to decimetre scale. While multiple occurrences of metasedimentary rocks were recorded within the volcanics, they are generally thin and discontinuous, with only one towards the base of the Formation of mappable width. The distribution of this unit is very localised and has a maximum thickness of 1550 meters.
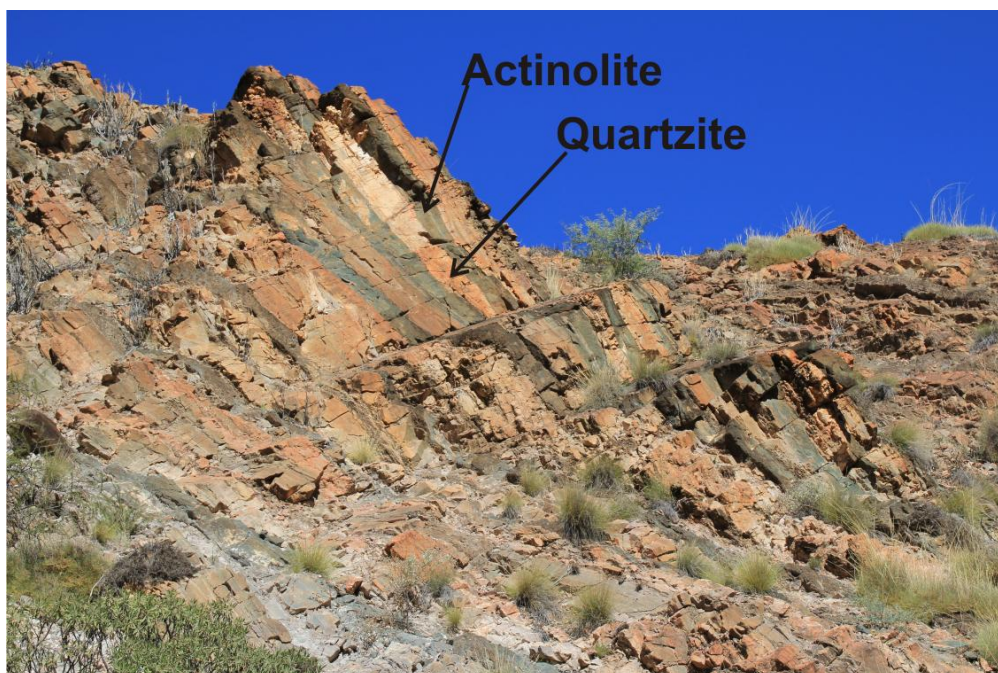
Figure 4: Photograph showing interbedded quartz and actinolite within the Wywyana Formation. Photo taken looking west.

HUMANITY SEAT FORMATION

The Humanity Seat Formation is a metamorphosed sedimentary unit comprised of quartz-dominated sands and lesser interbedded siltstones bedded at decimetre scale and was observed to locally and conformably overlie the Wooltana Volcanics. The upper third of the unit includes an interval of coarse-grained pebbly to conglomeritic beds. Crossbeds preserved as heavy mineral striations can be observed in the more quartz rich regions of this unit. Whilst prevalent in the west, there was no evidence found of this unit east of the central NE-SW fault present in the researched area. The thickness of this unit changes from an estimated thickness of just under 600 meters to the west of the western fault, to 250 meters to the east of the same fault (Figure 2).

LOWER ADELADIAN: STRUCTURE AND METAMORPHISM

THE WOODNAMOOKA FORMATION

The Woodnamooka Formation comformably ovelies the Humanity Seat Formation in the west of our mapping area and is in faulted contact with the Wooltana Volcanics in the east. By far the thickest sedimentary succession in the mapping area, the Woodnamooka association is comprised of 3 sub-units. These consist of a basal micaceous unit underlying a quartz and feldspar-rich ridge forming unit which underlies (and interfingers close to the Paralana Fault) and a finer grained unit. While the thickness of these units varies, as a whole, they appear to thicken towards the Paralana Fault.

The lower unit is a pelitic and psammopelitic metasediment characterised by coarse grained muscovite and biotite, which preserves a strong foliation defined by biotite, and localised cordierite porphyroblasts between 5 mm and 10 cm in size. We interpret the protolith of this unit to be interbedded muds, silts and sands within centimetre scale beds. It is in faulted contact with the Wooltana Volcanics on its lower boundary and directly abuts the Paralana Fault-altered rocks to the east. As the lowest region of this unit cannot be seen due to contacts with faults, the thickness of this unit cannot be determined.

The conformably overlying ridge forming unit (dubbed Mt Oliphant Arkose by Hansberry (2011) and Job (2011)) displays fine-scaled, interbedded sands and muds near the contact with the underlying unit and which gradually thicken to decimeter scale and become more quartz rich towards the top of the unit. The ridge forming component of this unit is the top 30 meters wherein the rock becomes significantly richer in quartz and feldspar, displays heavy mineral laminations and weathers orange. The thickness of

this unit is relatively consistent compared to the over and underlying units and equates to approximately 650 meters.

Conformably above the major ridge-forming unit is the thickest portion of the Woodnamooka Formation. This consists of inter-bedded sequences of finer sands and coarser sands with abundant, finer grained micas at centimetre scale bedding. Ripples and crossbeds are abundant within this unit preserved in bedding, becoming more prevalent towards the top of the unit. The thickness of this unit is highly variable with the thinnest recorded portion being 480m and approximately 1000m at its thickest.

BLUE MINE CONGLOMERATE

The Blue Mine Conglomerate as defined within our mapping area includes two conformable transitional packages from the Woodnamooka Formation into the rock unit known as the Blue Mine Conglomerate itself. The oldest of these transitional packages directly overlies the upper member of the Woodnamooka Formation. It is defined as an increase of the thickness of beds from cm scale to decimetre scale. This is accompanied by an increase in grain size and a drop in the mica content of the rock and the appearance of discrete decimetre scale coarse sand to pebble beds.

The upper boundary of these transitional packages is marked by the first appearance of centimetre sized clasts within the conglomerate beds. However, this gradational boundary does not contain the distinctive, angular K-feldspar clasts distinctive of the Blue Mine Conglomerate as clasts are predominantly sub-rounded fragments of quartz, iron oxide nodules, sand and siltstone. Graded bedding from course clasts to fine silts can be readily observed in this transitional package. Both of these

transitional packages gradually thin until they pinch out 500 meters east of Arkaroola Village (Figure 2).

The Blue Mine Conglomerate itself is a immature conglomerate comprised of angular clasts of K-feldspar and quartz. It is predominantly clast supported with a sand to fine mud matrix with decimetre to meter scale bedding. Cross beds can be observed through the entirety of Blue Mine Conglomerate and the transitional units. The total thickness of this unit

Map-scale Structure

FAULTS

There are 3 faults that cross cut the research area (Figure 2). The largest of these is the Paralana Fault, running along the eastern edge of the mapping area (Figure 2). Within our mapping area the Paralana Fault is north-south trending damage zone of fault gouge and disrupted stratigraphy, 40 to 100 meters in width which has strongly influenced local topography. Fault alteration appears as silica flooding, production of tremolite marbles, and chlorite alteration. Low angle, west dipping fault structures were observed very close to the eastern margin of the fault damage zone.The presence of these low angle structures is cause for investigation as the Paralana Fault has previously been interpreted to be a high angle thrust (Paul *et al.* 1999).

The second two faults, designated West Fault and Central Fault (Figure 2 & 3), appear to be relatively minor and not overly continuous from the structural map compiled. The West Fault cannot be seen to continue into the Humanity Seat Formation and the Central Fault terminates on contact with the Woodnamooka Formation (Figure 2). These faults strike parallel (NE-SW) to each other and no sense of movement

indicators were observed. However, due to map patterns, they are both interpreted to be normal during deposition with a later reverse component during basin inversion. Both appear to be steeply dipping as they both cut directly across topography. The strike of these faults also appears fairly parallel to the axial planes of the dominant fabric in the region and the axial planes of the regional folds.
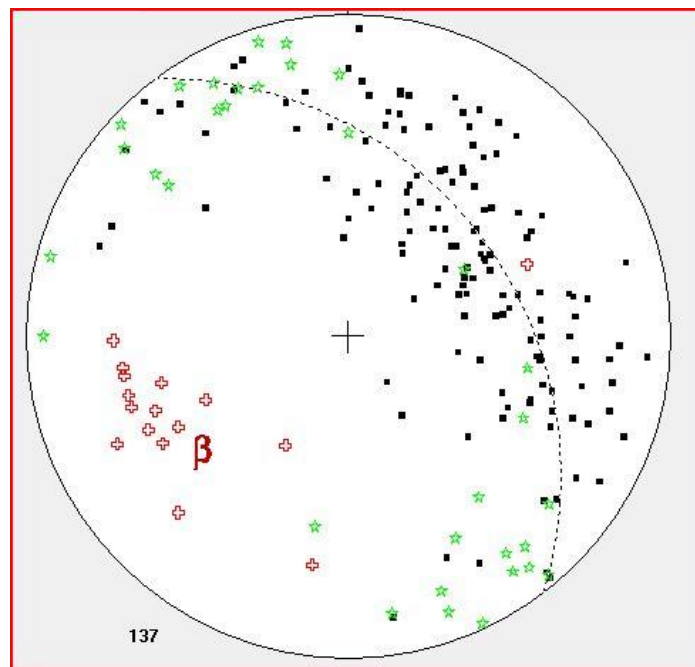
Figure 5: Stereonet displaying poles to bedding orientation (black squares), poles to principal foliation orientation (green stars) and cleavage bedding intersection lineations (red crosses). The calculated girdle represents an average cross sectional plane of the regional folds.

Folds

Three major folds have been observed within the research area, which appear to affect all units below the and including Blue Mine Conglomerate. All three of these are upright with NE/SW trending axial surfaces and hinges plunging towards the SW (Figure 5). The NW most fold appears to be the tightest of the three and the inter-limb angles of the folds appears to become greater moving to the SE (Figure 3) and tighter moving down stratigraphy. Further evidence for the style of this folding can be seen

close to the hinge of the western most syncline where outcrop scale parasitic folds can be observed within the Humanity Seat Formation (Figure 6). These parasitic folds can also be seen to be folding an earlier fabric which is parallel to bedding, in some cases into crenulations.

Figure 6: Outcrop scale parasitic fold (S0 shown by dotted line) within the Humanity Seat Formation Near the hinge of the western synform. Photo taken looking south east.

More folding can be observed close to the fault damage zone of the Paralana Fault. These folds have a different orientation to those of the major folds and axial planes in a similar orientation to the low angle fault structure in the same location suggesting that these are related to movement on these faults. The dominant regional fabric axial planar to the kilometre scale folds in the region can be seen to be folded around the hinges of these smaller folds (Figure 7). It is therefore interpreted that these folds and structures are the result further deformation prior to the inversion event which formed the larger folds.

LOWER ADELADIAN: STRUCTURE AND METAMORPHISM

Metamorphism

The most striking feature of the metamorphism in the region is the apparent increase in grade progressing down through the stratigraphic column. Micas become more abundant and coarser-grained and the abundance of cordierite rich zones and the size of the cordierite porphyroblasts increases.
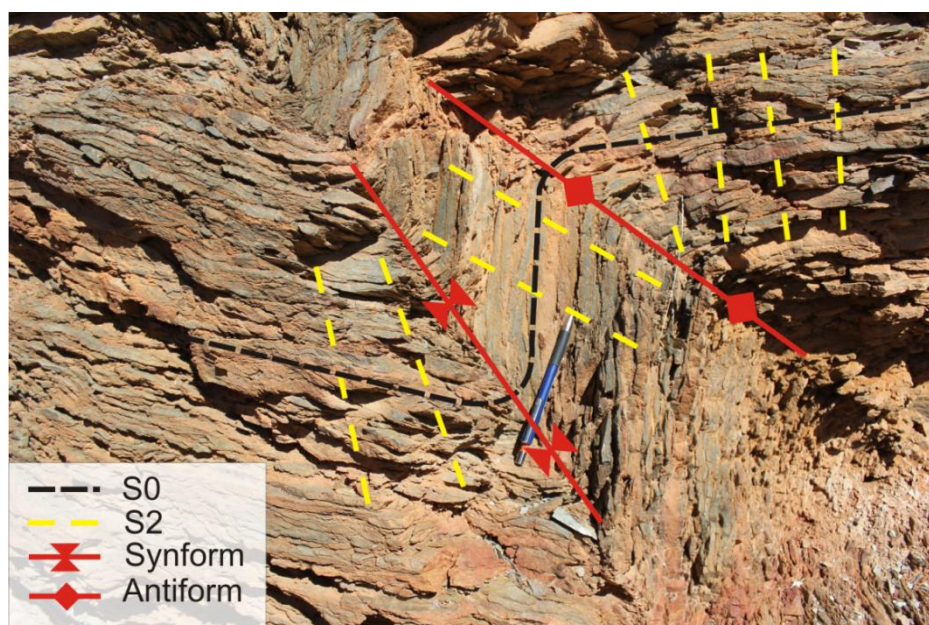
Figure 7: Photo of fault related folds near the Paralana Fault. S0 the original bedding and S2 is the pervasive regional fabric shown to be folded by these small scale folds. Photo taken looking south.

The dominant fabric in the rock is comprised of muscovite and biotite and wraps around the cordierite porphyroblasts (Figure 8). An older fabric is locally preserved in particular in the hinge zones of folds and within cordierite porphyroblasts. On closer inspection of the cordierite, mica inclusions within the porphyroblast appear aligned in an orientation at a high angle to the dominant fabric. There also appear to be compositional changes within some of these porphyroblasts which are also aligned with this elongation of micas and other minerals included within the cordierite. This earlier fabric is always seen to be parallel to bedding (Figure 8A). Finally, there appear to be multiple stages of cordierite growth with the earlier stage being a more prismatic,

inclusion-poor zone in the crystal and the later, a more inclusion-rich zone exhibiting

secular twinning (Figure 8 B).
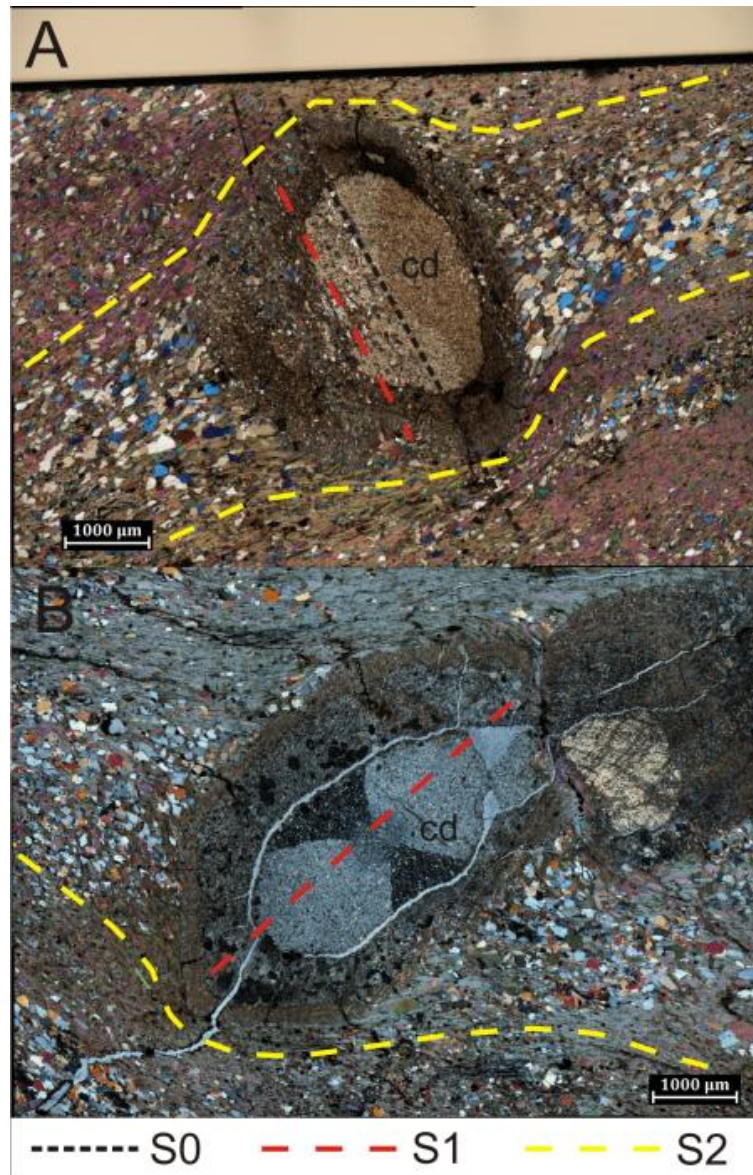
Figure 8: Both a and b show a corderite porphyroblast under cross-polarised light situated in a thin section cut from sample R-15. A shows the relationship between bedding, the S1 fabric and S2 fabric (regional fabric). B shows the relationship between S1 and S2 as well as the secular twinning in the cordierite.

The margins of the cordierite porphyroblasts show a rim of different mineralogy which

appears to be a reaction rim which also shows inclusions of minerals which are also

aligned with the older fabric preserved within the cordierite (Figure 8). The dominant

fabric in the region, comprised primarily of muscovite and biotite, can be seen wrapping around the porphyroblasts, and hence its development is interpreted to post date the second phase of cordierite growth.

Monazite is abundant both within the porphyroblasts and within the matrix of both samples. The monazite grains observed in thin section under SEM, range from 5 μm to 20μm with most grains lying towards the smaller end of this size range. For this reason, the thin sections acquired were unsuitable for in situ analysis. The average size of monazite grains may also have been the reason that so few monazites were able to be separated.

Monazite Geochronology

GRAIN MORPHOLOGY

None of the separated monazites display coherent crystal form. All have embayments on the grain margins and contain inclusions of both host rock minerals and other metamorphic phase minerals. This indicates that at least the outer regions grew around and over existing minerals within the rock. These textures are typical of metamorphic monazite. The metamorphic nature of the monazite grains is reinforced by the presence of biotite inclusions within some of the monazites (Figure 9A) which are interpreted to be derived from an earlier metamorphic event.

BSE images from both samples indicates complex zoning present in almost all of the monazite grains mounted. Broadly speaking, the zoning styles present in the BSE images can be placed into 3 categories; a central patchy zone (Figures 9A, 10A and 11A) an outer, broadly more homogenous and slightly concentrically zoned region and

27
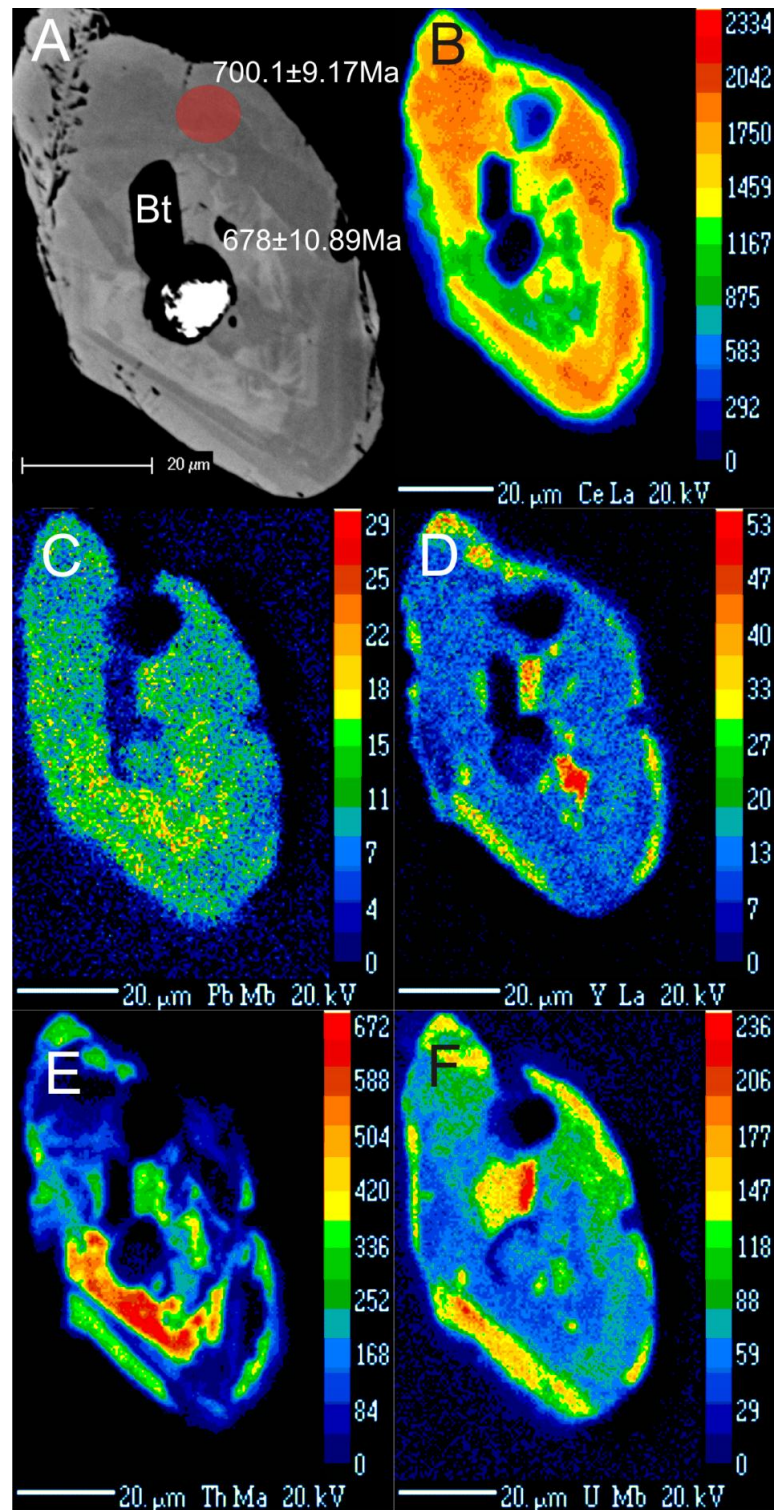
Figure 9: A shows a BSE image of a metamorphic monazite from sample R-15, $^{206}Pb/^{238}U$ ages estimates of each laser spot, and the presence of a biotite inclusion. Images B, C, D, E and F show EPMA compositional maps of the grain shown in A of Ce, Pb, Y, Th and U respectively. The central spot can be seen to be overlapping a zone of heterogeneous Pb and U which is likely the cause for the younger age.
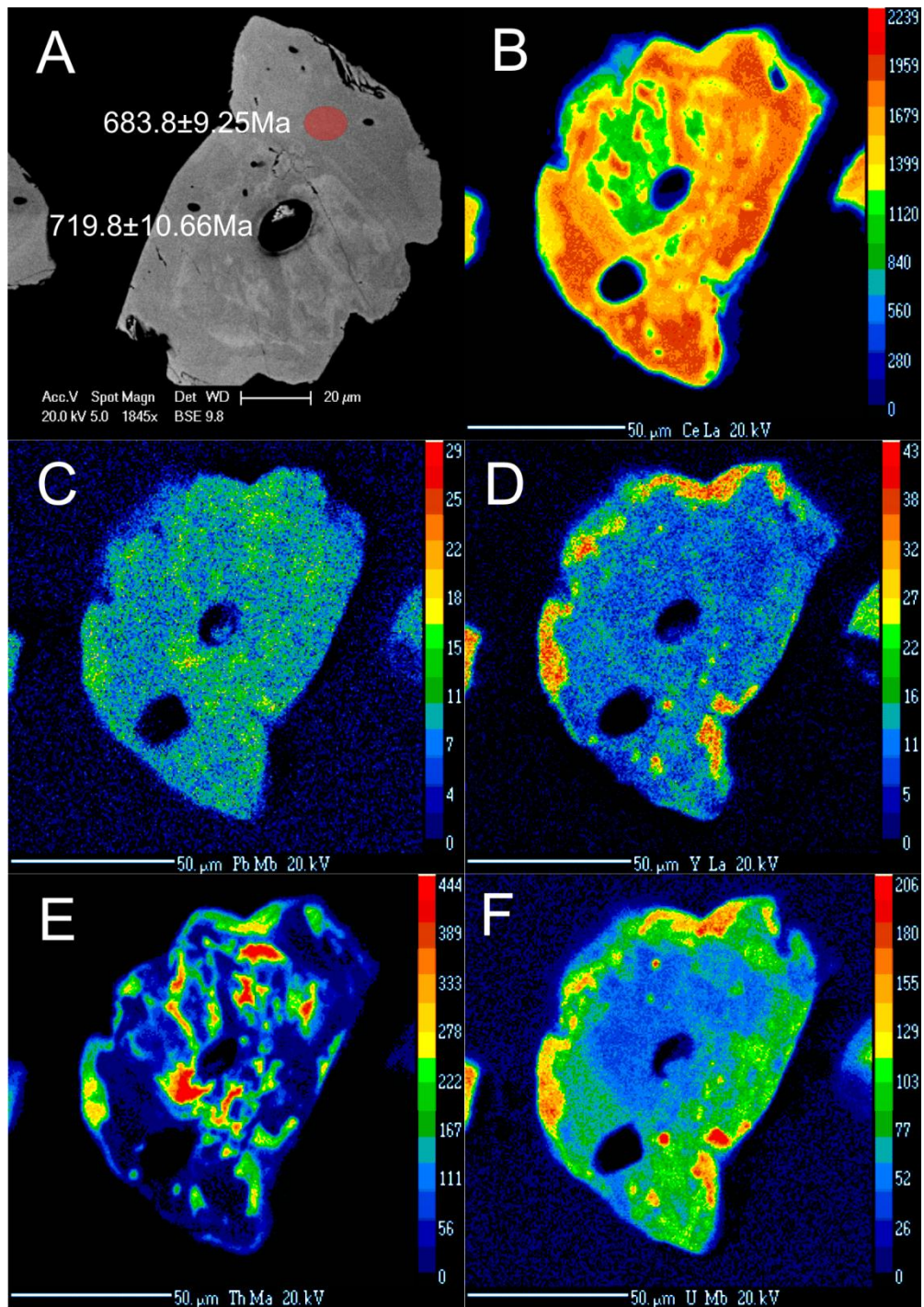
Figure 10: A shows an BSE image of a metamorphic monazite grain from sample R-12 with the $^{206}Pb/^{238}U$ dates of each laser spot. Of particular note are the embayments around the crystal margins indicating growth around other existing minerals indicative of metamorphic monazite. Images B, C, D, E and F show EPMA compositional maps of the grain shown in A of Ce, Pb, Y, Th and U respectively
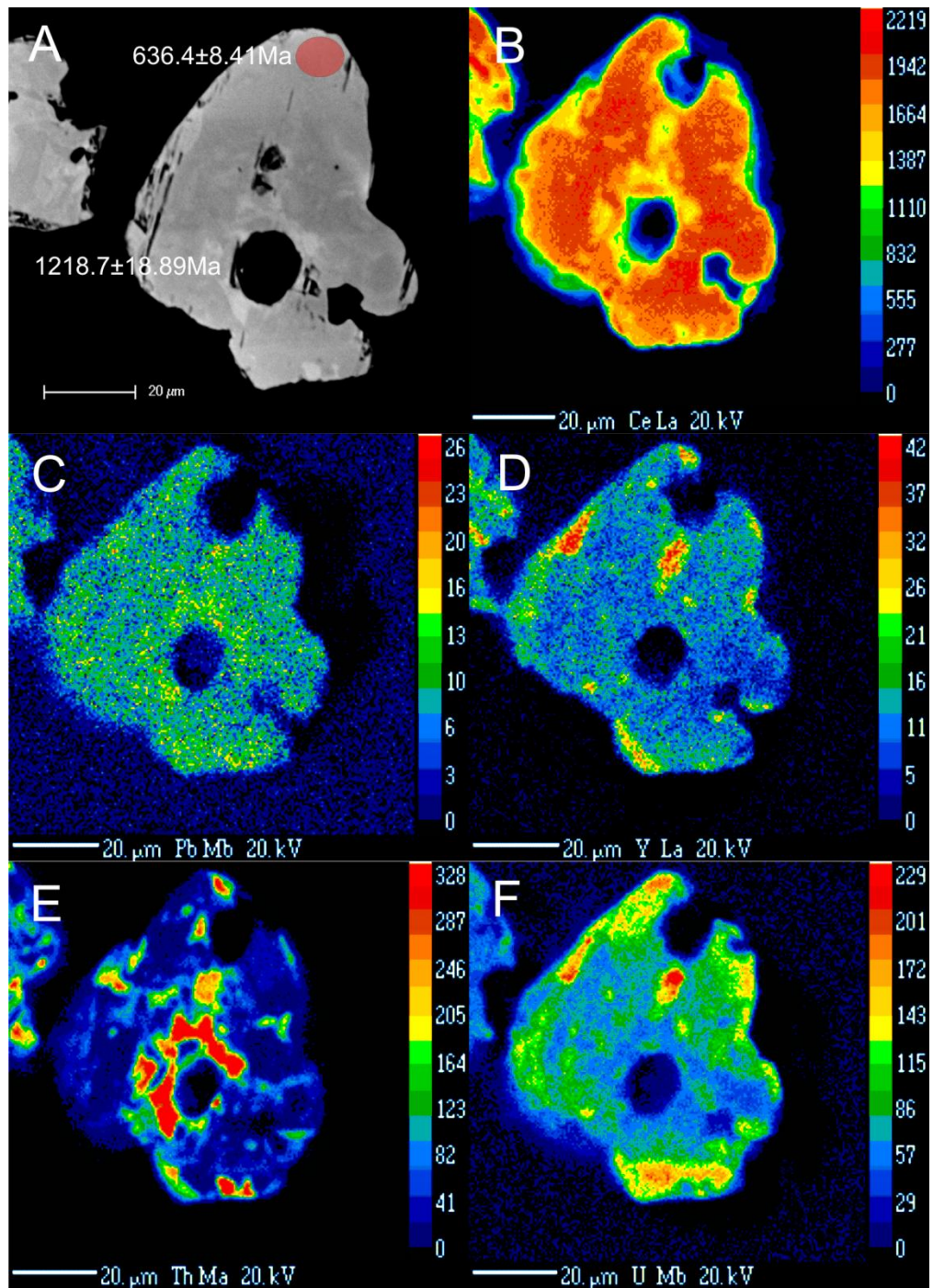
Figure 11: Image A consists of a BSE image showing a detrital monazite grain from sample R-15 that has been overgrown by a later monazite growth event. $^{206}Pb/^{238}U$ age estimates of both laser spots are shown and embayments around crystal margin indicate that the second growth event occurred within the host rock. Images B, C, D, E and F show EPMA compositional maps of the grain shown in A of Ce, Pb, Y, Th and U respectively
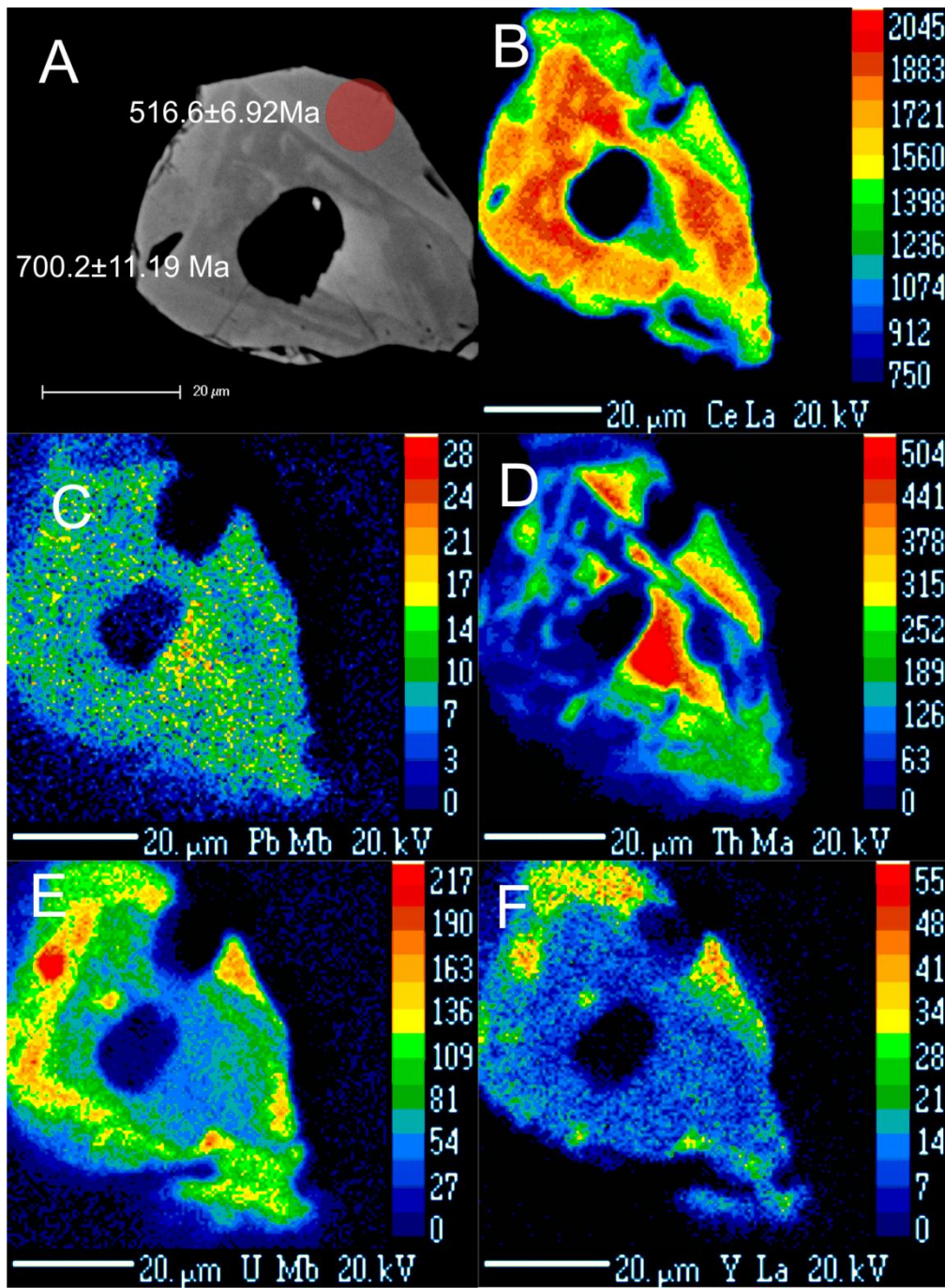
Figure 12: A shows a BSE image of a metamorphic monazite from sample R-15 and $^{206}Pb/^{238}U$ ages estimates of each laser spot. This grain likely shows clear evidence of three compositional domains within a single monazite grain. Images B, C, D, E and F show EPMA compositional maps of the grain shown in A of Ce, Pb, Th, U and Y respectively

a more reflective rim. All these zones may be present in one grain or a grain may only preserve one of these zonation styles.

Maps generated by the EPMA shed more light on these compositional domains. In general, the zoning present on the BSE images is most accurately mirrored by Ce compositional zoning particularly the concentric zoning. Zones of high Th and Pb tend to correspond well to the zones that appear patchy in the BSE images but this is not always the case. In general, Pb is patchy throughout the grains, however variations in Pb are very slight and there are often zones of patchy high U in the centre of grains. The most consistent pattern that emerges in the analysis of the EPMA compositional maps is the spike in abundance of U around the grain rims. This appears consistent through most of the mapped grains (Figures 9, 10, 11 and 12 (B,C,D,E and F)

LA ICP-MS U-PB DATA

Much of this data derived from LA-ICP-MS is not concordant or appears to be smeared along the Concordia line. The discordant data appears to be "pulled" compositionally towards a younger, possibly Palaeozoic age (Figures 13 and 14). The data was "cleaned" through analysis of EPMA images and BSE images and data derived from laser pits which clearly overlapped compositional zoning was discarded. This significantly increased the average concordance of the data and increased the resolution of the two age peaks. The data for this is presented in the following section.

SAMPLE R-12

We collected data from 53 spots on 35 grains separated from R-12. When frequency histograms and Concordia diagrams were generated from these data, vague peaks were

seen at aproximatly 700 and 650 (Figure 13) as well as a lower number of points with a low concordance and high error preserving an interpreted Mesoproterozic age. However, some of the data appears quite discordant or smeared along the Concordia line and therefore new plots were calculated after having discounted data coming from laser spots that clearly mixed compositional zones.

The filtered data, when plotted on Concordia diagrams, shows clustering of ages around approximately 700 Ma and 650 Ma as well as a further older ages that are in the Mesoproterozoic. The Mesoproterozoic ages are discordant and smeared over a period of 500 Ma and with large errors. The 700 Ma population appears more concordant although points are scattered above and below the Concordia line (Figure 14). The ages calculated appear smeared along the Concordia line over approximately 50 Ma (figure 13). The 650 Ma cluster is the tightest and most concordant of the three groups. Again ages appear smeared along the Concordia line between 600 Ma and 650 Ma (figure 13). Ranged from oldest to youngest, the calculated weighted average ^{206}Pb/^{239}U ages of these is these are 705.2 ± 7.4 Ma and 644.2 ± 8.0 Ma (Figure 14).

SAMPLE R-15

Data for sample R-15 was collected from 68 spots over 41 separated monazite grains. The Concordia plots generated from the raw data display a smear of ages from approximately 800 Ma down to about 600 Ma. The generated probability density plot displays four, poorly defined age peaks at 706, 640, 590, and 503 Ma. The average concordance of the ages derived is also significantly lower than that of R-12. Again data derived from laser spots of obviously mixed ages was discounted and Concordia diagrams, probability density plots and weighted average plots where re-calculated.
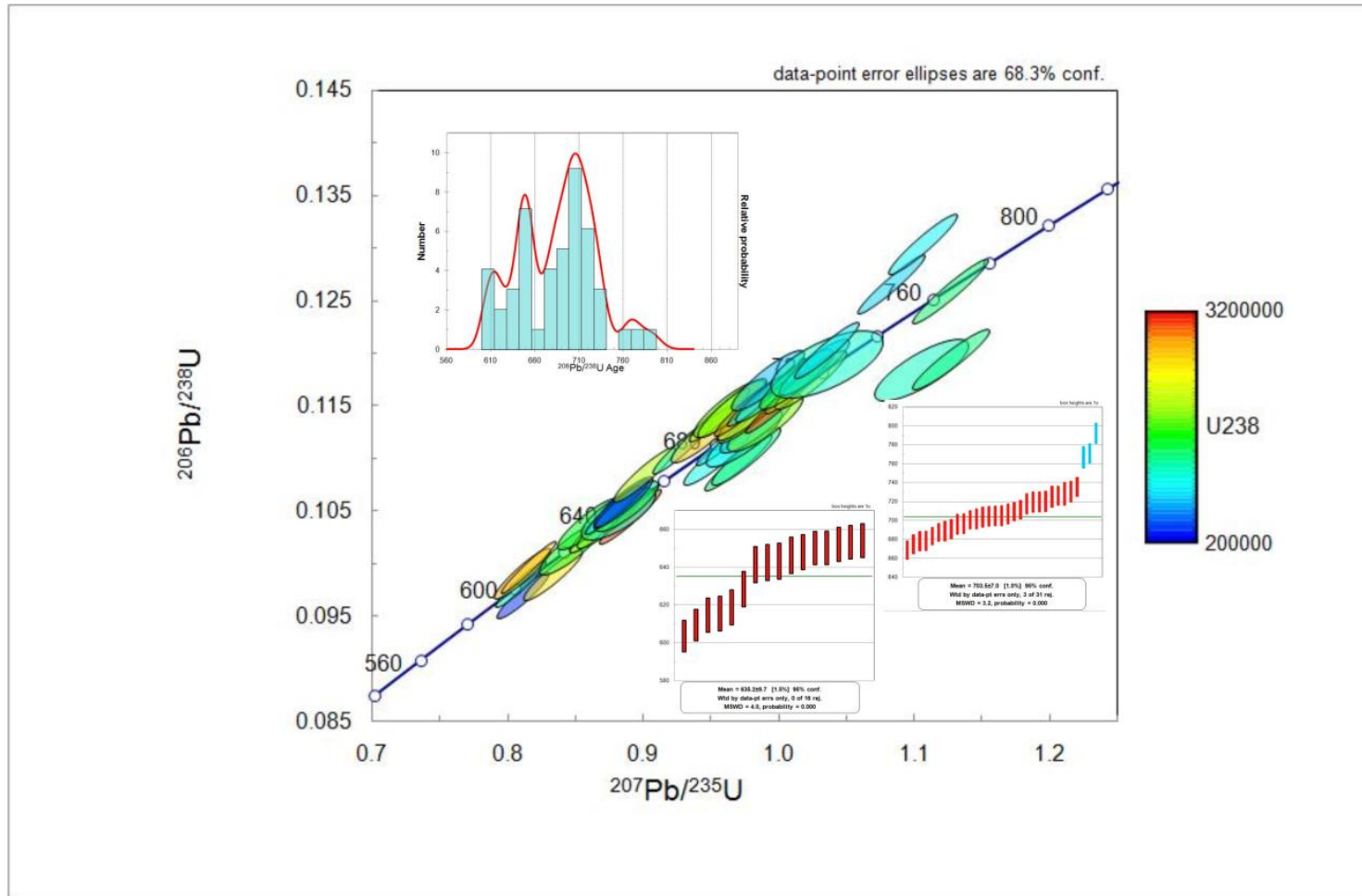
Figure 13: A Concordia plot of all LA-ICP-MS data from sample R-12 showing ^{238}U content for each data point. Ages estimates are smeared along the Concordia line from approximately 600 Ma to around 780 Ma with two vague clusters around 705 Ma and 640 Ma. Insert of a Probability density plot for all ^{206}Pb/^{238}U data is shown in the top left-hand corner with the weighted averages of the peaks in incepts in the lower right. The weighted averages are 635.2±9.7 Ma (95% conf.) and 703.5±7.0 Ma (95% conf.)
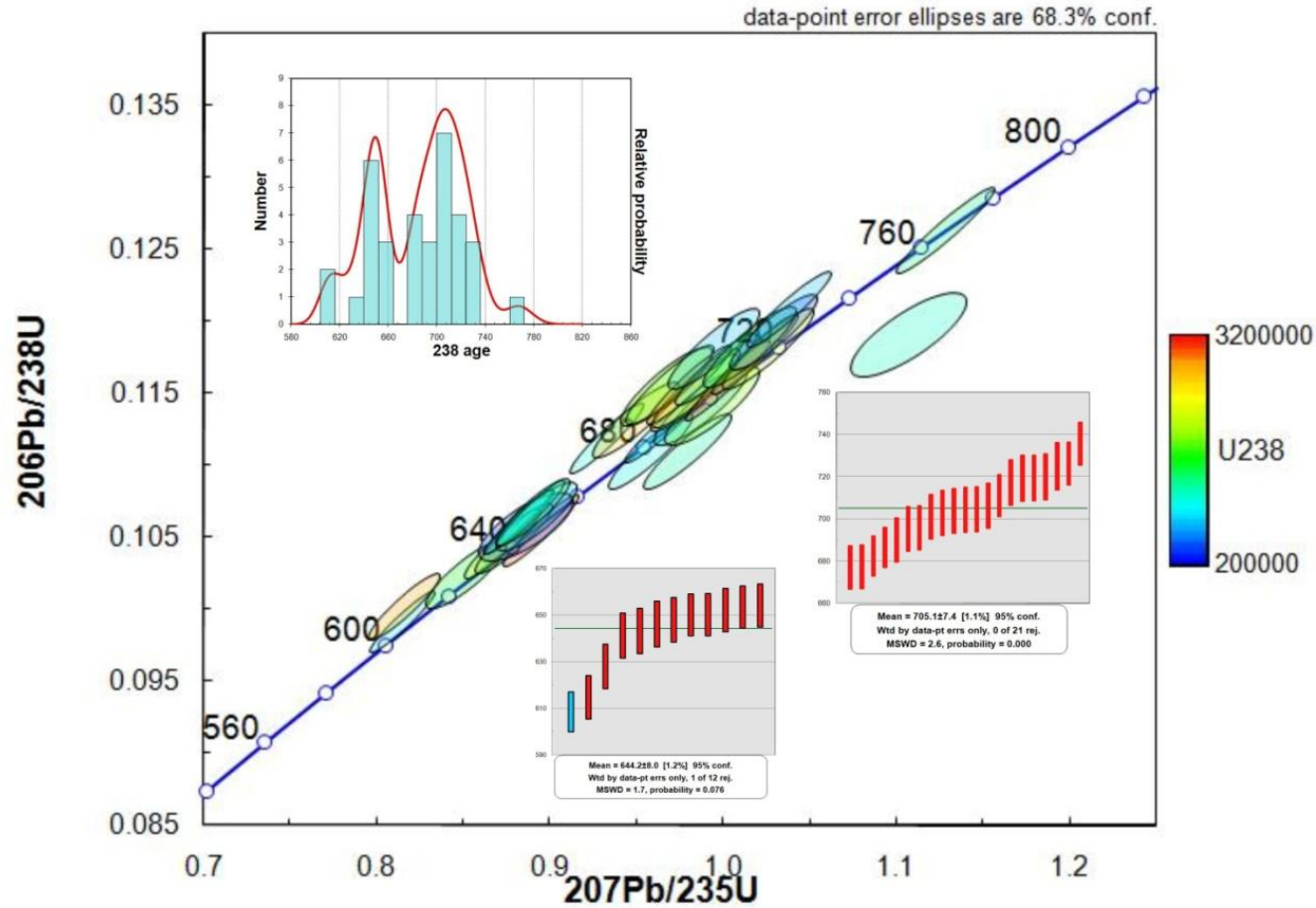
Figure 14: A concordia plot of data LA-ICP-MS U/Pb data after data filtering was conducted showing [238]U content of each data point from R-12. There are two significantly better defined clusters at approximately 705 and 640 with far less discordant and reversely discordant data. Two very well defined peaks can be seen in probability density plot (top left) and the weighted averages plots for these two peaks can be seen in the inserts in the lower right. Weighted average [206]Pb/[238]U age estimates for the two clusters are 644.2±8.0Ma (95% conf.) and 705.1±7.4 Ma (95% conf.).
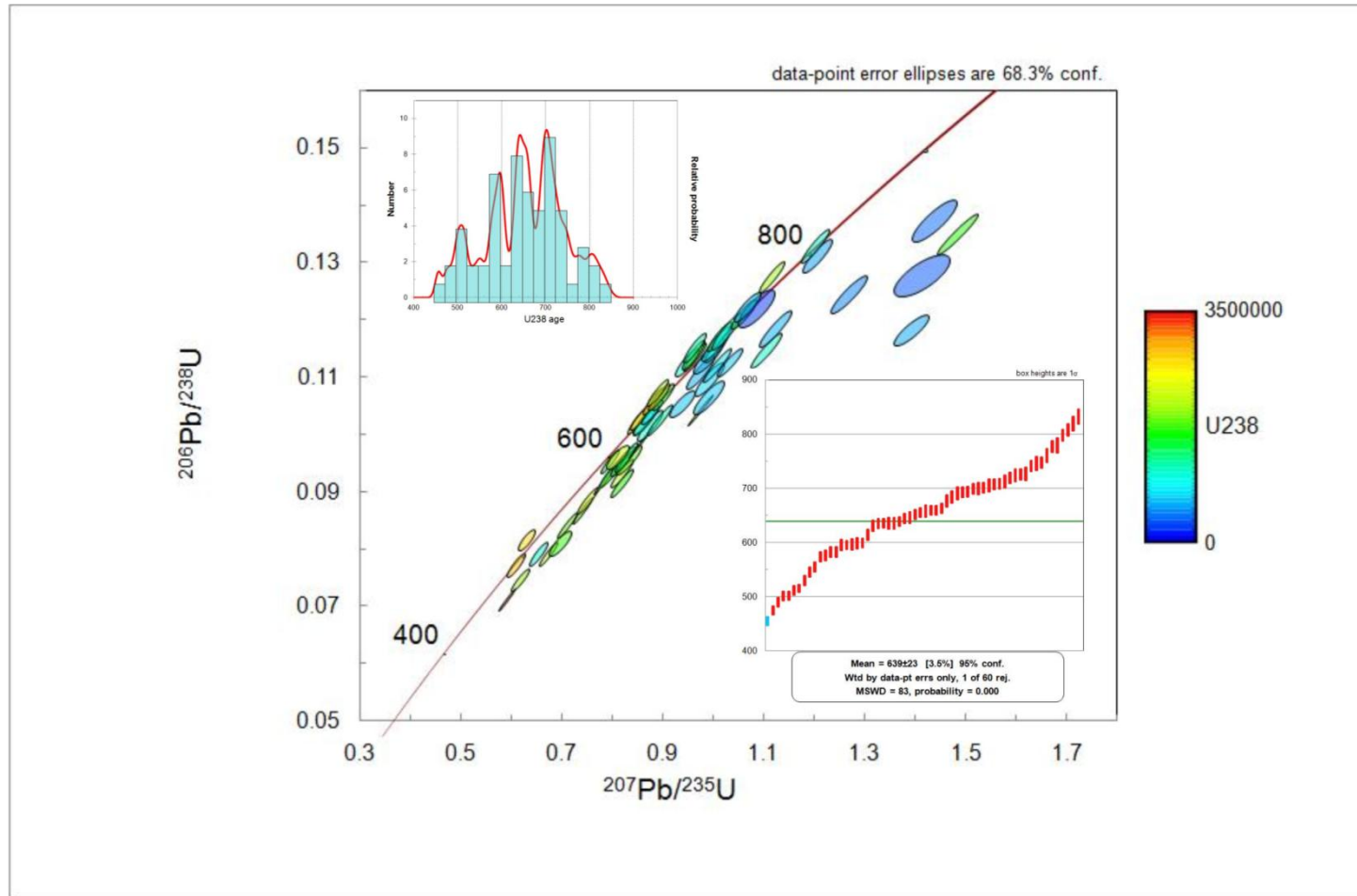
Figure 15: A Concordia plot of all LA-ICP-MS data from sample R-15 Showing [238]U content of each data point. Ages estimates are smeared along the Concordia line from approximately 600Ma to around 780 Ma with no definitive clusters present. Much of the data is severally discordant with the intercept being somewhere in the Palaeozoic (approximately 300 Ma). The probability density plot (insert in top left corner) shows some vague peaks in ages but nothing definitive. Calculated weighted average for [206]Pb/[238]U age estimates is 639±23 Ma (95% conf.) (plot in lower right insert).
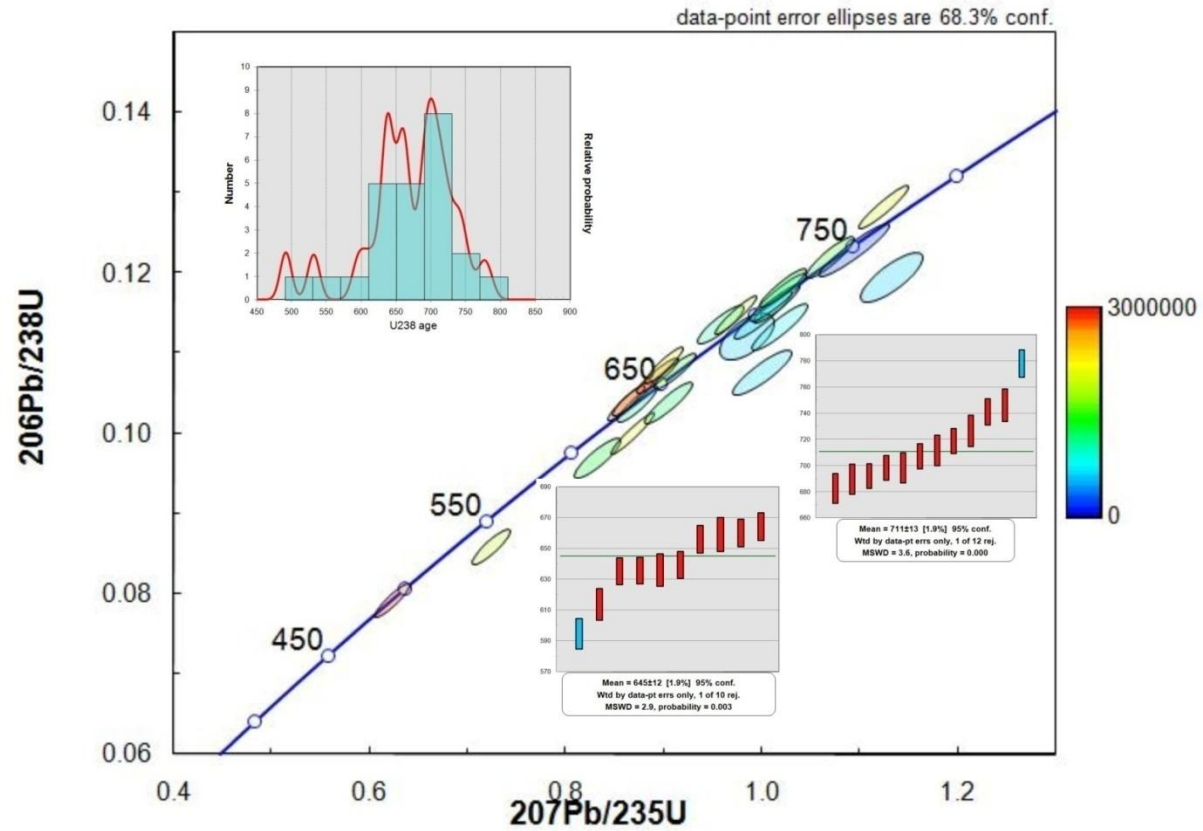
Figure 16: A Concordia plot of Filtered LA-ICP-MS data from sample R-15 Showing ^{238}U content of each data point. Ages estimates are smeared along the Concordia line from approximately 600 Ma to around 780 Ma with slight clustering around 700 Ma and 650 Ma. Concordance of this sample is lower than R-12 and the Discordia trend also appears to intersect the Concordia line somewhere in the vicinity of 300 Ma. The probability density plot (top left) still displays 2 distinct age clusters. The weighted average plots (bottom right) ^{206}Pb/^{238}U age estimate of these peaks are 645±12 Ma and 711±13 Ma.

LOWER ADELADIAN: STRUCTURE AND METAMORPHISM

The Concordia diagram for the filtered data does not show the same distinct grouping at 700 and 640 as R-12. While there is still clearly a discordant population in the Mesoproterozoic, the young data appears smeared between approximately 750 Ma and 600 Ma (Figure 15). The discordant data appears to line around a line of Discordia which likely intercepts the Concordia line somewhere in the Paliozoic. However, probability density plots of $^{206}Pb/^{239}U$ ages show two distinct peaks at similar points to those of R12 (Figure 15). The weighted average age of these peaks are 645 ± 12 Ma and 711 ± 13 Ma (Figure 15) There is one concordant point at with a $^{206}Pb/^{239}U$ age of 491.3 ± 8.2 Ma (Figure 15). Finally, R15 shows a broad linear trend of an increase in uranium as the $^{206}Pb/^{239}U$ age decreases before data cleaning. However, subsequent to data cleaning, this trend becomes less apparent but there does appear to be a slight spike in U in the 650 Ma cluster of ages.

Figure 12, taken from sample R-15 clearly shows s the presence of a high uranium zone around the rim of the grain. The laser spot overlaps this outer rim and a central homogenous zone so the age produced is likely a mix of both of these domains.

DISCUSSION

Significance of the Metamorphic Monazite Ages.

The LA-ICP-MS results for monazites separated from the Woodnamooka Formation yield three clear ages of monazite growth, two of which are likely Neoproterozoic growth or re-setting events, and the third being an earlier Mesoproterozoic event in sediment source rocks. For the purposes of this study the age estimates yielded by R-12 will be used as the timing for the monazite growth or resetting events as they have the lower error.

LOWER ADELADIAN: STRUCTURE AND METAMORPHISM

Pre-850 Ma ^{206}Pb/^{283}U age estimates are interpreted as relic detrital monazite, due to the 827± 6 Ma interpreted age of the Wooltana Volcanics and the estimated 840 Ma age of the Paralana Quartzite (Preiss 2000). As the Woodnamooka Formation is stratigraphically above both of these units, any monazite predating the Wooltana Volcanics and the Paralana Quartzite could not have grown after deposition of the sampled rock and therefore must be a remnant detrital monazite derived from the sedimentary source of the Woodnamooka Formation. Data points showing these ages are generally very discordant and have a very large error ellipse. Many appear partially reset and show extensive, patchy alteration typical of fluid interaction (Figure 11) (Teufel & Heinrich 1997, Harlov *et al.* 2011, Williams *et al.* 2011). It is therefore possible that the younger age populations are the result of fluid resetting or fluid mediate growth.

The first major monazite growth phase within the Woodnamoka Formation is recorded by the peak seen at 700-710 Ma observed in both samples. The age interpreted to be the most accurate for this growth event is the ^{206}Pb/^{283}U age estimate of 705.2 ± 7.4 Ma derived from sample R-12, as the error value is lower than that provided for that age peak provided by sample R-15. Previous geochronological work on monazites from the Central Flinders Ranges within the overlying Sturtian and Marinoan sequences yielded authigenic monazite. These produced a spread of ages ranging from around 700 Ma to 300 Ma (maximum age of 680 ± 23 Ma using Th-U-total Pb methods). This could lead to the younger age populations present in the Woodnamooka Formation monazites to be interpreted as authigenic. However, monazites from R-12 and R-15 can be seen to contain inclusions of biotite (Figure 9), indicating that the host rock had already undergone low grade metamorphism prior to monazite growth. This, coupled with the

presence of discrete growth events defined by age populations distinctive of monazite growth at amphibolites facies and above (Bosch *et al.* 2002, Kohn & Malloy 2004, Carson *et al.* 2008, Krenn *et al.* 2008, Zhang *et al.* 2012, Berman *et al.* 2013), means that the possibility that these monazites grew authigenically can be discounted. The $^{206}Pb/^{238}U$ age estimate also coincides with the onset of the third rift event in the development of the Adelaide Rift Complex which has the potential to increase the geothermal gradient through crustal thinning. These factors also allow us to interpret the 705.2 ± 7.4 Ma age estimate as metamorphic monazite growth.

The second monazite growth event occurred at 644.2 ± 8 Ma. Spots preserving this age are generally taken from fairly compositional homogenous zones within the monazite grains whereas the 700 Ma ages occur both in homogenous zones and in the patchy central zones (Figures 9A and 10 A). This suggests that the 644 Ma age is a fluid assisted growth event and hence, some of the 700 Ma age zones appear fluid altered. The 644 Ma age coincides with the onset of the dexteral shearing phase in the development within the Adelaide Rift Complex (Preiss 2000). It is possible that this period of active tectonics re-mobilised fluids within the sedimentary pile allowing for the second monazite growth event.

It is likely that there is also a third, younger monazite growth event not recorded in the data. Where laser spots overlap high U zones on the crystal rim, the result is a younger, slightly discordant age estimate (Figure 12, A and E). This is most likely to be the result of mixing of a 644 or 705 Ma age with a younger age domain within the crystal. More evidence of this later growth event is seen in the unfiltered data sets for R-12 and R-15. A clear discordance pattern can be seen to be pulling the monazite ages towards an age in the Palaeozoic (Figure 13 and 15). This still occurs in the filtered data

but is less apparent due to data derived from laser spots that obviously mixed age domains being removed (Figures 14 and 16).

Implications for tectonic evolution.

BASIN DEVELOPMENT

The Paralana Quartzite and the Wywyana formations are inferred to have been deposited in a shallow marine environment prior to the major rifting during the break up of Rodinia (Figure 15A). The Wooltana Volcanics are regarded as the marker for the onset of this major rifting in the region and this provides an answer to the apparently restricted locations of the Wooltana Volcanics. Activation of the Central Fault as a normal fault is interpreted to have created a localised basin in the hanging wall in which the volcanics were deposited (Figure 15B). Calc silicates within the volcanic are compositionaly similar to the Wywyana formation and are therefore interpreted to have been deposited in periods between volcanic eruptions and derived from the same sedimentary source as the Wywyana formation.

Further extension caused the activation of the West Fault as a normal fault creating a larger basin which would have been subsequently filled with the Humanity Seat Formation (Figure 15C). This explains the change in stratigraphic thickness of the Humanity Seat Formation thinning significantly to the east of the west fault (Figures 2 and 3).

Significant stratigraphic thickening and a general coarsening of sedimentary material within both the Woodnamooka Formation and the Blue Mine Conglomerate towards the Paralana Fault can be seen in our research area (Figure 2). It is therefore

interpreted that both the Woodnamooka Formation and the Blue Mine Conglomerate were deposited in a basin controlled by normal motion on the Paralana Fault.

A distinct change in the composition and size of clasts can be observed moving stratigraphically up from the Woodnamooka Formation, through the transitional packages and into the Blue Mine Conglomerate . The lowermost of the transitional packages shows an increase in the energy of the environment from that of the Woodnamooka Formation with the occurrence of decimetre scale graded beds. The second transitional package records an increase in clast size. The compositions of these clasts are predominantly iron oxides, portions of silt and sandstone and quartz, all of which are well rounded. They are interpreted to be sourced from a peneplain- like weathering surface and the movement of surface regolith into the newly formed basin. The Blue Mine Conglomerate itself contains feldspar clasts, likely sourced from a granitic body. As the only proximal source of igneous intrusive materials are located within the local basement, it probable that this is the source of the sediments. The transitional packages and the Blue Mine Conglomerate can therefore be interpreted to record a history of the late stage of the local basin development caused by movement on the Paralana Fault. The first transitional package likely records an increase in uplift and topographic relief caused by movement on the fault. The second transitional package can be interpreted to be the first major uplift on the fault with the transport of the old weathering surface material into the basin. The Deposition of the Blue Mine Conglomerate most probably coincides with the exposure of the regional basement in the hanging wall of the Paralana Fault.
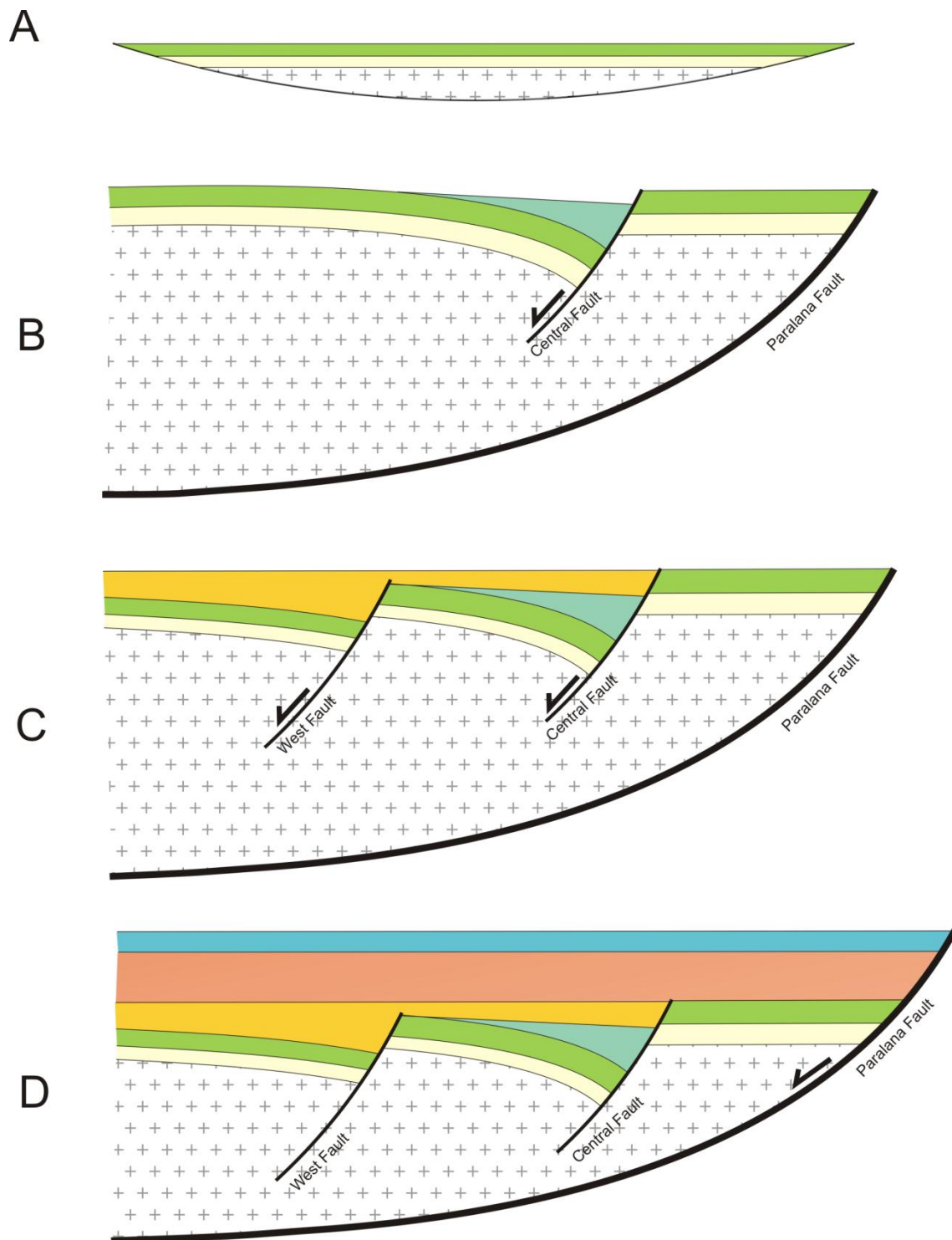
Figure 17: This figure shows an interpreted cross section of local basin development in the researched area. A shows the shallow marine environment during the first stage of deposition. B shows activation of the central fault and subsequent emplacement of the Wooltana Volcanics. C shows activation of the West Fault and the structural controls on the location of the Humanity Seat Formation. D shows normal movement on the Paralana Fault and subsequent deposition of the Woodnamoka Formation and the Blue Mine Conglomerate.

LOWER ADELADIAN: STRUCTURE AND METAMORPHISM

This local basin was then overlain of the remainder of the Burra Group leaving a depositional gap between approximately 760 Ma with the deposition of the Skillogallee Dolomite and 710 Ma with the deposition of the Sturtian Bolla Bollana Formation. The deposition of the Bolla Bollana coincides with the onset of the third major rift phase in the development of the Adelaide Rift Complex (Preiss 2000), a process generally associated with high heat flow(McKenzie 1978). As the minimum possible age for the Sturtian Glaciation is constrained to at 680 ± 23 (U-Th-total Pb geochronology) Ma by Mahan *et al.* (2010) our $^{206}Pb/^{239}U$ age estimate of 705.2 ± 7.4 Ma is interpreted to record a metamorphic, monazite growth event associated with the rift phase and burial.

As no higher grade metamorphic minerals can be observed within the study region, it is interpreted by this study that the cordierite growth reflects the peak metamorphism of the region. Hence, the growth of cordierite is likely represented as the 705 Ma age derived from the monazite. A bedding parallel fabric defined by biotite is observed within the cordierite porphyroblasts in figure 8. This is interpreted to be a flattening fabric formed during the pro-grade portion of 705 Ma metamorphic event and is most likely related to the burial.

This age constraint places a sedimentary pile of approximately 5 km (figure 16) on top of the region of the Woodnomoka Formation from which the samples were obtained. Given the stability of cordierite in rocks of this composition at this depth we can assume a minimum temperature of 500 ^{o}C. This gives a minimum geothermal gradient of around 100 ^{o}C/Km at the time of metamorphism; a far higher geothermal gradient than previously estimated (Sandiford *et al.* 1998a, McLaren *et al.* 2002). It is likely that the high heat producing rocks of the Mt Painter Inlier coupled with the rifting event are responsible for this very high geothermal gradient as the interpreted geothermal gradient is higher than either factor could produce alone.

LOWER ADELADIAN: STRUCTURE AND METAMORPHISM

DEFORMATION

The folds in our research area are upright with relatively low inter-limb angles. The folds are present in the Blue Mine Conglomerate but inter-limb angle tighten significantly in the lower stratigraphies (Figure 3) and are absent in higher stratigraphies. The axial traces of the regional folds are parallel to the strike of both the West Fault and the Central Fault and are therefore interpreted to be related to the formation of the regional folds.

Sedimentary drape over the Western and Central Faults and into discrete basins between faults could form broad fold structures. This coupled with local gradual compression during deposition due to a compressional jog derived from two strike slip faults (one of which is Paralana) approaching each other is one possible explanation for the structures observed in the research area. This would result in tightening of these broad sag folds into the structures observable in the field. The upper age limit of this interpretation is constrained by the deposition of the Opaminda Formation and the Wortupa Quartzite as these units do not show evidence of the folds preserved in our research area. This would place the sampled sediments at a burial depth of approximately 1300 meters at a minimum geothermal gradient of 370 ^{o}C/km (Figure 18). A geothermal gradient this high would have lead to partial to complete melting of lower crustal rocks of which there is no evidence. Therefore it is unlikely that the fold structures in the region were caused by this mechanism.

Another theory pertaining to the formation of the structures is that they were folded significantly after the deposition of the overlying units. It is possible that through strain partitioning, that the Lower Burra and Callana beds developed complex folding during the shortening event that produced the large Arkaroola Syncline to the south of the research area and are possibly parasitic "s" folds (Figure 3) to this kilometre scale fold. This is a well documented phenomenon (Frehner & Schmalholz 2006) often preserved in beds that provide
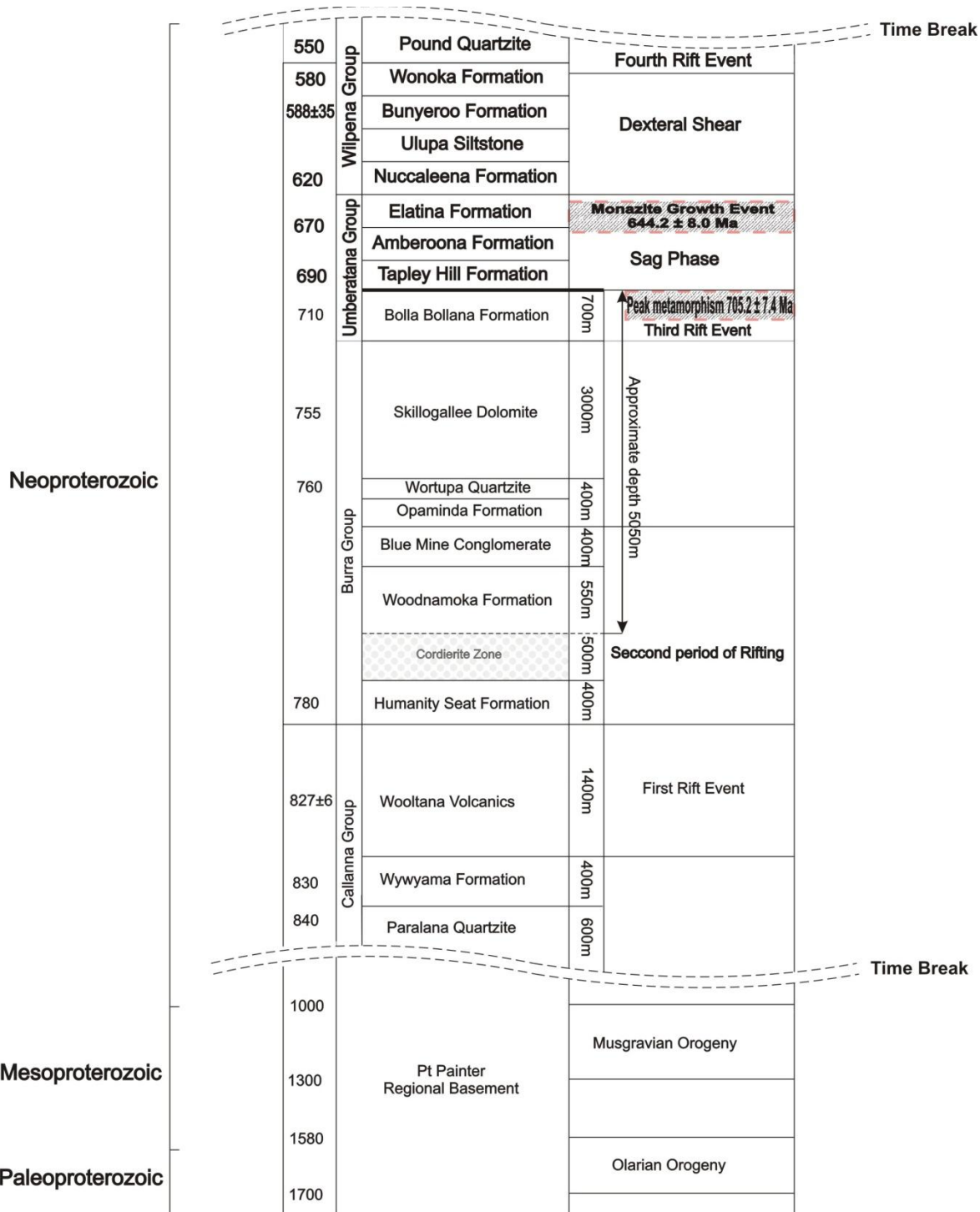
Figure 18: A time-space plot showing the development history of the Adelaide Rift Complex as it pertains to the Arkaroola Region. The First column contains approximate ages of events in millions of years. The second column contains lithologies including stratigraphic thicknesses of the Callana and Burra Groups. The final column contains major tectonic and metamorphic events during and prior to the development of the Adelaide Rift Complex (Coats *et al.* 1969, Powell *et al.* 1994, Preiss 2000, Mitchell *et al.* 2002).

less resistance to deformation such as silts, clays and fine grained carbonates. The Oppaminda formation (comprised primarily of carbonates) provides a possible slip surface to allow for this partitioning of deformation. This is interpreted to be the most likely mechanism for the formation of the folds within our mapping area.

As the Pound Quartzite, locally the youngest unit in the Adelaidean sequence (Preiss 2000), is deformed by the Arkaroola syncline (Coats *et al.* 1969), the age of deformation must be subsequent to the conclusions of the Adleaidean Rift Complex Development. The only monazite data from this study that may point to the timing of the deformation is the presence of the high U growth event, forming the rim of many of the sample monazite grains (Figures 9E, 10E, 11E and 12E). However there are no dates confined to this monazite growth event. Laser spots which overlap this high U zone tend to be discordant with the discordia trend appearing to intersect the concordia line at a mid to early Palaeozoic age. It can therefore be tentatively interpreted that the rocks were deformed during the Mid-Palaeozoic Alice Springs Orgoeny rather than the Cambrian-Ordovician Delamerian Orogeny as previously thought. However there is very little evidence for this and, due to lack of monazites of sufficient size in thin section to undertake in situ dating, more research is required to test this hypothesis fully.

Outcrops near the Paralana Fault Damage zone contain evidence for further deformation subsequent to the formation of the regional fabric and hence the major folding event. Small fault related folds confined to discrete beds within 50 meters of the Paralana Fault damage zone can be seen to fold the regional fabric. Low angle, narrow (4cm) brittle structures can also be observed in the outcrop with a dip similar to that of the axial plains of the small folds. This can be interpreted to be a history of recent basin inversion and uplift from a relatively ductile environment in which the folds where formed, into a brittle

environment in which the low angle fault structures would have formed. This is most likely Palaeozoic or Mesozoic deformation and is the other possible cause of the young age, toward which the discordant monazites are being pulled.

CONCLUSIONS

From the data derived from analysis of monazite, coupled with field observations and thin-section examination several conclusions can be drawn. It is clear that there are two monazite growth events within the region; the first at 705.2±7.4 Ma and the second at at 644.2±8 Ma. The first is interpreted to coincide with cordierite growth triggered by the deposition of Sturtian sediments during the third period of tectonic rifting during the formation of the Adelaide Rift complex. This post dates the formation of a flattening fabric within the Woodnamoka Formation. The cause of the second monazite growth event is not so easily interpreted. It is however likely that it is due to fluid assisted metamorphism conceding and possibly caused by a period of dextral shear in the region.

The second deformation event, responsible for the formation of kilometre scale folds and overprinting of the older flattening fabric by a newer compressional fabric in the Lower Burra and Callana Groups remains unconstrained. However, based on the inferred parasitic relationship between the folds observed in our research area and the Arkaroola Syncline, the folding event can be interpreted to have occurred after the deposition of the Pound Quartzite which is folded by the Arkaroola Syncline. Further geochronological work on this fabric using in-situ monazite dating techniques possibly in conjunction with $^{40}Ar/^{39}Ar$ and K/Ar dating on micas and amphiboles may be able to constrain the timing of the second deformation event.

LOWER ADELADIAN: STRUCTURE AND METAMORPHISM

ACKNOWLEDGMENTS

REFERENCES

BAKKER R. J. & ELBURG M. A. 2006. A magmatic-hydrothermal transition in Arkaroola (northern Flinders Ranges, South Australia): From diopside-titanite pegmatites to hematite-quartz growth. *Contributions to Mineralogy and Petrology* **152**, 541-569.

BERMAN R. G., SANBORN-BARRIE M., RAYNER N. & WHALEN J. 2013. The tectonometamorphic evolution of Southampton Island, Nunavut: Insight from petrologic modeling and in situ SHRIMP geochronology of multiple episodes of monazite growth. *Precambrian Research* **232**, 140-166.

BOSCH D., HAMMOR D., BRUGUIER O., CABY R. & LUCK J.-M. 2002. Monazite "in situ" 207Pb/206Pb geochronology using a small geometry high-resolution ion probe. Application to Archaean and Proterozoic rocks. *Chemical Geology* **184**, 151-165.

BRUGGER J., ANSERMETM S. & PRING A. 2003. Uranium minerals from Mt Painter, norther Flinders Ranges, South Australia. *Australian Journal Of Mineralogy* **9**, 15-31.

BRUGGER J., LONG N., MCPHAIL D. C. & PLIMER I. 2005. An active amagmatic hydrothermal system: The Paralana hot springs, Northern Flinders Ranges, South Australia. *Chemical Geology* **222**, 35-64.

BRUGGER J., WÜLSER P. A. & FODEN J. 2011. Genesis and preservation of a uranium-rich paleozoic epithermal system with a surface expression (northern Flinders Ranges, South Australia): Radiogenic heat driving regional hydrothermal circulation over geological timescales. *Astrobiology* **11**, 499-508.

CARSON C. J., WORDEN K. E., SCRIMGEOUR I. R. & STERN R. A. 2008. The Palaeoproterozoic evolution of the Litchfield Province, western Pine Creek Orogen, northern Australia: Insight from SHRIMP U–Pb zircon and in situ monazite geochronology. *Precambrian Research* **166**, 145-167.

COATS R., P., HORWITZ R., C., CRAWFORD A., R., CAMPANA B. & THATCHER D. 1969. *Mount Painter Province*. Department of Mines, S.A.

DREXEL J. F., PREISS W. V. & PARKER A. 1993. *The Geology of South Australia* (Vol. 54). Mines and Energy, South Australia, Geological Survey of South Australia.

LOWER ADELADIAN: STRUCTURE AND METAMORPHISM

ELBURG M. A., ANDERSEN T., BONS P. D., SIMONSEN S. L. & WEISHEIT A. 2013. New constraints on Phanerozoic magmatic and hydrothermal events in the Mt Painter Province, South Australia. *Gondwana Research*.

ELBURG M. A., BONS P. D., DOUGHERTY-PAGE J., JANKA C. E., NEUMANN N. & SCHAEFER B. 2001. Age and metasomatic alteration of the Mt Neill Granite at Nooldoonooldoona Waterhole, Mt Painter Inlier, South Australia. *Australian Journal of Earth Sciences* **48**, 721-730.

ELBURG M. A., BONS P. D., FODEN J. & BRUGGER J. 2003. A newly defined Late Ordovician magmatic-thermal event in the Mt Painter Province, northern Flinders Ranges, South Australia. *Australian Journal of Earth Sciences* **50**, 611-631.

FODEN J., ELBURG M. A., DOUGHERTY-PAGE J. & BURTT A. 2006. The timing and duration of the Delamerian orogeny: Correlation with the Ross Orogen and implications for Gondwana assembly. *Journal of Geology* **114**, 189-210.

FOSTER G., GIBSON H. D., PARRISH R., HORSTWOOD M., FRASER J. & TINDLE A. 2002. Textural, chemical and isotopic insights into the nature and behaviour of metamorphic monazite. *Chemical Geology* **191**, 183-207.

FREHNER M. & SCHMALHOLZ S. M. 2006. Numerical simulations of parasitic folding in multilayers. *Journal of Structural Geology* **28**, 1647-1657.

GIBSON H. D., CARR S. D., BROWN R. L. & HAMILTON M. A. 2004. Correlations between chemical and age domains in monazite, and metamorphic reactions involving major pelitic phases: An integration of ID-TIMS and SHRIMP geochronology with Y-Th-U X-ray mapping. *Chemical Geology* **211**, 237-260.

HANSBERRY R. 2011. *Tectonic evolution of the Arkaroola Basin: implications for the development of the Adelaide Rift Complex. Geolgoy*. University of Adelaide.

HARLOV D. E., WIRTH R. & HETHERINGTON C. J. 2011. Fluid-mediated partial alteration in monazite: The role of coupled dissolution-reprecipitation in element redistribution and mass transfer. *Contributions to Mineralogy and Petrology* **162**, 329-348.

HOWARD K. E., HAND M., BAROVICH K. M., PAYNE J. L. & BELOUSOVA E. A. 2011. U-Pb, Lu-Hf and Sm-Nd isotopic constraints on provenance and depositional timing of metasedimentary rocks in the western Gawler Craton: Implications for Proterozoic reconstruction models. *Precambrian Research* **184**, 43-62.

JACKSON S. E., PEARSON N. J., GRIFFIN W. L. & BELOUSOVA E. A. 2004. The application of laser ablation-inductively coupled plasma-mass spectrometry to in situ U-Pb zircon geochronology. *Chemical Geology* **211**, 47-69.

JOB A. 2011. *Evolution of the basal Adelaidean in the Northern Flinders Ranges: deposition, provenance and deformation of the Callana and Lower Burra Groups.* University of Adelaide.

KOHN M. J. & MALLOY M. A. 2004. Formation of monazite via prograde metamorphic reactions among common silicates: implications for age determinations. *Geochimica et Cosmochimica Acta* **68**, 101-113.

KOŠLER J. 2007. Laser ablation ICP—MS — a new dating tool in Earth science. *Proceedings of the Geologists' Association* **118**, 19-24.

KRENN E., USTASZEWSKI K. & FINGER F. 2008. Detrital and newly formed metamorphic monazite in amphibolite-facies metapelites from the Motajica Massif, Bosnia. *Chemical Geology* **254**, 164-174.

LUDWIG L., R. 2012. *Isoplot 3.75: A Geochronological Toolkit for Microsoft Excel*. **5:** 75. Berkely Geochronology Center.

MAHAN K. H., WERNICKE B. P. & JERCINOVIC M. J. 2010. Th-U-total Pb geochronology of authigenic monazite in the Adelaide rift complex, South Australia, and implications for the age of the type Sturtian and Marinoan glacial deposits. *Earth and Planetary Science Letters* **289**, 76-86.

MARTINS L., VLACH S. R. F. & JANASI V. D. A. 2009. Reaction microtextures of monazite: Correlation between chemical and age domains in the Nazaré Paulista migmatite, SE Brazil. *Chemical Geology* **261**, 271-285.

MCKENZIE D. 1978. Active tectonics of the Alpine—Himalayan belt: the Aegean Sea and surrounding regions. *Geophysical Journal of the Royal Astronomical Society* **55**, 217-254.

MCLAREN S., DUNLAP W. J., SANDIFORD M. & MCDOUGALL I. 2002. Thermochronology of high heat-producing crust at Mount Painter, South Australia: Implications for tectonic reactivation of continental interiors. *Tectonics* **21**, 2-1 - 2-18.

MCLAREN S., SANDIFORD M., DUNLAP W. J., SCRIMGEOUR I., CLOSEZ D. & EDGOOSE C. 2009. Distribution of Palaeozoic reworking in the Western Arunta Region and northwestern Amadeus Basin from 40Ar/39Ar thermochronology: implications for the evolution of intracratonic basins. *Basin Research* **21**, 315-334.

MCLAREN S., SANDIFORD M., POWELL R., NEUMANN N. & WOODHEAD J. 2006. Palaeozoic intraplate crustal anatexis in the mount painter province, South Australia: Timing, thermal budgets and the role of crustal heat production. *Journal of Petrology* **47**, 2281-2302.

MILDREN S. D. & SANDIFORD M. 1995. Heat refraction and low-pressure metamorphism in the northern Flinders Ranges, South Australia. *Australian Journal of Earth Sciences* **42**, 241-247.

MITCHELL M. M., KOHN B. P., O'SULLIVAN P. B., HARTLEY M. J. & FOSTER D. A. 2002. Low-temperature thermochronology of the Mt Painter Province, South Australia. *Australian Journal of Earth Sciences* **49**, 551-563.

PAQUETTE J. L. & TIEPOLO M. 2007. High resolution (5 μm) U–Th–Pb isotope dating of monazite with excimer laser ablation (ELA)-ICPMS. *Chemical Geology* **240**, 222-237.

PARRISH R. R. 1990. U-Pb dating of monazite and its application to geological problems. *Canadian Journal of Earth Sciences* **27**, 1431-1450.

PAUL E., FLOTTMANN T. & SANDIFORD M. 1999. Structural geometry and controls on basement-involved deformation in the northern Flinders Ranges, Adelaide Fold Belt, South Australia. *Australian Journal of Earth Sciences* **46**, 343-354.

POWELL C. M., PREISS W. V., GATEHOUSE C. G., KRAPEZ B. & LI Z. X. 1994. South Australian record of a Rodinian epicontinental basin and its mid-neoproterozoic breakup (~700 Ma) to form the Palaeo-Pacific Ocean. *Tectonophysics* **237**, 113-140.

PREISS W. V. 2000. The Adelaide Geosyncline of South Australia and its significance in Neoproterozoic continental reconstruction. *Precambrian Research* **100**, 21-63.

QUIGLEY M., SANDIFORD M., FIFIELD K. & ALIMANOVIC A. 2007. Bedrock erosion and relief production in the northern Flinders Ranges, Australia. *Earth Surface Processes and Landforms* **32**, 929-944.

SANDIFORD M., HAND M. & MCLAREN S. 1998a. High geothermal gradient metamorphism during thermal subsidence. *Earth and Planetary Science Letters* **163**, 149-165.

LOWER ADELADIAN: STRUCTURE AND METAMORPHISM

SANDIFORD M., PAUL E. & FLOTTMANN T. 1998b. Sedimentary thickness variations and deformation intensity during basin inversion in the Flinders Ranges, South Australia. *Journal of Structural Geology* **20**, 1721-1731.

TEUFEL S. & HEINRICH W. 1997. Partial resetting of the U-Pb isotope system in monazite through hydrothermal experiments: An SEM and U-Pb isotope study. *Chemical Geology* **137**, 273-281.

WEISHEIT A., BONS P. D. & ELBURG M. A. 2013. Long-lived crustal-scale fluid flow: The hydrothermal mega-breccia of Hidden Valley, Mt. Painter Inlier, South Australia. *International Journal of Earth Sciences* **102**, 1219-1236.

WILLIAMS M. L., JERCINOVIC M. J., HARLOV D. E., BUDZYŃ B. & HETHERINGTON C. J. 2011. Resetting monazite ages during fluid-related alteration. *Chemical Geology* **283**, 218-225.

ZHANG C., VAN ROERMUND H., ZHANG L. & SPIERS C. 2012. A polyphase metamorphic evolution for the Xitieshan paragneiss of the north Qaidam UHP metamorphic belt, western China: In-situ EMP monazite- and U–Pb zircon SHRIMP dating. *Lithos* **136–139**, 27-45.

APPENDIX A: EXTENDED METHODS.

Mapping

The research area mapped is bound on the southern side by the Arkaroola village road, on the west and north by the Echo Camp backtrack and on the east by north-south trending ridges governed by the Paralana Fault. The total area mapped is approximately 16 square kilometres Structural mapping of the research area was conducted over twenty one consecutive days with a further two days in the field at a later date with the help of supervisors. Field transects collecting bedding and foliation information using a compass clinometers and observations on rock types coupled with the use of Quickbird aerial photography of the region at 1:10 000 scale were also used as a mapping aid. All observation data and interpretations made while in the field were noted. Lithological boundaries and structural features were inferred from analysis of structural data, field observations, and interpretation of the aerial images.

LOWER ADELADIAN: STRUCTURE AND METAMORPHISM

Sample collection and preparation

Fifteen oriented rock samples were taken in the mapping area representing each of the mapped units. Representative outcrops where selected based upon weathering, mineralogy and ease of hand specimen removal. Samples of in situ portions of outcrop were removed using a sledge hammer after being photographed and having their dip and dip direction marked and recorded.

Orientated thin sections of these samples were cut perpendicular to foliation for tectonic fabric analysis using a rock saw, upper surface and desired face marked and then sent to Pontifex for grinding and polishing. These were subsequently carbon coated after examination on transmitted light microscope in preparation for analysis on the scanning electron microscope.

The remainder of the sample was crushed using a jaw crusher and disk mill consecutively and the 79µm to 450µm fraction was separated using a sieve. Separated monazites were then obtained by first using panning to remove all light material. Secondly magnetic franze wath then used to separate the portion magnetic between .5 nT and .8 nT. The desired fraction was then placed in heavy liquids which were then repeatedly stirred and drained until no more material was observed to sink through the solution. The heavy fraction of this sample was then subjected to further separation on the Franz gradually increasing the magnetism in increments of .1 nT. After each run through the Franz, the magnetic portion was observed and the fraction contain monazite (.6nT and .7nT) was retained. Monazites from this fraction were then handpicked under a reflected light microscope and mounted in epoxy resin. The resulting blocks were polished by hand on a wet, fine emery disc (not rotating) and the placed on a cloth lap for 10 minutes to finalise the polish. Mounts were then carbon coated in preparation for analysis under scanning electron microscope and electron microprobe.

LOWER ADELADIAN: STRUCTURE AND METAMORPHISM

Sample analysis

Thin sections cut from were viewed under transmitted light microscope and photos were taken of futures of interested under both cross polarised light and normal light. Multiple fabrics and evidence of multiple stages of metamorphism were examined, identified and recorded. Thin sections were then observed under a scanning electron microscope (XL40) using back scatter electron analysis to determine the plausibility of in-situ dating of monazite. Unfortunately, all monazites located in thin section under the SEM were too small (<10μm) to be of use for in-situ dating through Laser ablation inductively coupled plasma mass spectrometry (LA ICP-MS).

Few of the selected samples contained sufficient monazite for analysis. From these we selected samples R-12 and R-15 for analysis due to their monazite yield potential to contain monazite of different generations preserved in porphyroblasts. The two samples were taken from widely separated locations within a comparable stratigraphic location (Figure 2). Back scatter electron (BSE) images were obtained of individual grains in each mount using a XL40 scanning electron microscope (SEM) for compositional zoning analysis. Compositional maps of Al, Ca, Ce, Fe, K, Mg, P, Pb, Si, Th, Ti, U, and Y of selected monazite grains were generated using an SX5 Electon Micro probe (EPMA).

LA ICP-MS was selected as the dating method for the separated monazites as it allows for the fast and relatively accurate dating of a large quantity of sample when compared to electron microprobe and SHRIMP techniques (Košler 2007). While not possessed of the accuracy of SHRIMP dating due to the size of the laser spot and error inherent in the ablation of a portion of the sample, the laser ablation method is still possessed of the accuracy required (Paquette & Tiepolo 2007) to constrain the differences in ages that have been hypothesised. U-Pb isotopic analyses where gathered using a New Wave 213nm Nd-YAG laser in an He ablation

atmosphere coupled to an Agilent 7500cs ICP-MS. 30s of gas blank was analysed followed by 60s of analysis during monazite ablation. Prior to ablation, the laser was fired for 10s with the shutter closed to allow for beam stabilization. The beam diameter was approximately 12 μm at sample surface. Isotopes concentrations analysed were 204Pb for 10ms, 206Pb for 15ms, 207Pb for 30ms, and 238 U for 15ms.

Ages of monazites were calculated using the real-time correction program 'Glitter' developed at Macquarie University, Sydney (Jackson et al. 2004). The correction of the U-Pb fraction was achieved through the use of the MAdel monazite standard (TIMS normalisation data: 207Pb/206Pb=490.7 Ma, 206Pb/238U=514.8 Ma and 207Pb/235U=510.4 Ma). Prior to unknown analysis, corrected age accuracy was confirmed through analysis of an in-house monazite standard with a reported 206Pb/238Pb age of 450.2 ± 3.4 Ma.

The results attained from LA ICP-MS were analysed in conjunction with the BSE images and the EPMA compositional maps to determine the effect of possible laser spot overlap upon the ages calculated by Glitter. Through this, it was possible to discount data that clearly derived from mixed compositional domains within the monazite crystal. These mixed compositional zones were specifically looking for zones where spots overlapped Pb and U compositionaly heterogeneous zones. These grains were then compared to BSE images and common patterens were used to filter possibly mixed spots on non EPMA imaged grains. Data was plotted on concordia diagrams, frequency diagrams and weighted averaged diagrams and ages calculated using Isoplot (version3) (Ludwig 2012)

APPENDIX B: R-12 RAW LA-ICP-MS DATA

R-12: Raw Concordia Data

Analysis_#	Pb207/U235		Pb206/U238		rho	Concordancy	Pb206/U238	error	Pb207/U235	error	U238
R1201	0.82014	0.01325	0.10076	0.00158	0.970602	102	618.9	9.23	608.1	7.39	2595358
R1202	1.12743	0.01842	0.12635	0.00198	0.959157	100	767	11.33	766.5	8.79	1367374
R1203	0.97881	0.01668	0.11105	0.00174	0.91946	98	678.9	10.09	693	8.56	1207555
R1203D	1.10766	0.01664	0.13075	0.00186	0.946944	96	792.2	10.61	757	8.01	889513
R1204	4.80103	0.07643	0.31586	0.00493	0.980444	98	1769.5	24.14	1785.1	13.38	1344785
R1205	0.97297	0.01608	0.11044	0.00173	0.947836	98	675.3	10.03	690	8.28	1363198
R1205D	1.08422	0.01601	0.12701	0.0018	0.959756	97	770.8	10.32	745.7	7.8	765446
R1206	0.95714	0.01618	0.11098	0.00173	0.922143	100	678.5	10.06	681.8	8.39	979394
R1206D	0.98709	0.01472	0.11634	0.00166	0.956815	98	709.5	9.57	697.2	7.52	811744
R1207	1.00218	0.01618	0.11593	0.00181	0.967052	100	707.1	10.43	704.9	8.21	3073145
R1208	1.01755	0.01655	0.11778	0.00183	0.955295	101	717.8	10.58	712.7	8.33	2371692
R1209	1.12786	0.01865	0.12004	0.00187	0.942089	95	730.8	10.79	766.7	8.9	1302964
R1209D	0.88122	0.01324	0.10614	0.00151	0.946878	99	650.3	8.81	641.6	7.15	993318
R1210	0.89429	0.01457	0.10547	0.00164	0.954407	100	646.4	9.57	648.7	7.81	3066411
R1210W	1.03735	0.01558	0.1209	0.00172	0.94724	98	735.8	9.92	722.6	7.77	828483
R1211	0.97936	0.01604	0.11563	0.0018	0.950473	102	705.4	10.37	693.3	8.23	2862464
R1212	0.98342	0.01693	0.11535	0.00181	0.911471	101	703.8	10.46	695.4	8.67	2042071
R1213	3.59638	0.05827	0.26823	0.00416	0.957208	97	1531.8	21.16	1548.7	12.87	2489799
R1213D	0.96447	0.01434	0.11259	0.0016	0.955784	100	687.8	9.3	685.6	7.41	980534
R1214	0.81542	0.01357	0.10022	0.00155	0.929349	102	615.7	9.11	605.5	7.59	2828529

R1215	0.87184	0.01452	0.10463	0.00163	0.935409	101	641.5	9.49	636.6	7.87	2314894
R1215D	0.81637	0.01254	0.09819	0.0014	0.928219	100	603.8	8.23	606	7.01	313589
R1216	0.90425	0.01505	0.10938	0.0017	0.93382	102	669.1	9.89	654	8.02	2016964
R1216D	0.88086	0.01299	0.10612	0.00151	0.964889	99	650.2	8.79	641.4	7.01	1007037
R1217	0.8381	0.01404	0.10007	0.00155	0.924606	99	614.8	9.11	618.1	7.76	2490961
R1218	0.99398	0.01753	0.11814	0.00185	0.887913	103	719.8	10.66	700.7	8.93	705546
R1218D	0.93196	0.01403	0.11191	0.0016	0.949709	98	683.8	9.25	668.7	7.37	1137944
R1219	0.87836	0.01496	0.10496	0.00163	0.911811	101	643.4	9.52	640.1	8.09	1732719
R1220	1.02529	0.01735	0.11815	0.00183	0.915302	100	719.9	10.57	716.6	8.7	2169556
R1221	0.96873	0.01655	0.1156	0.0018	0.911422	103	705.2	10.37	687.8	8.54	1854274
R1221D	0.88783	0.01331	0.10668	0.00152	0.950413	99	653.4	8.87	645.2	7.16	367587
R1221W	0.88532	0.01787	0.10577	0.0016	0.749434	99	648.1	9.32	643.9	9.62	1099281
R1222	0.9826	0.01673	0.11505	0.00178	0.908687	101	702	10.32	694.9	8.57	2522630
R1223	0.98618	0.01764	0.11409	0.00178	0.872228	100	696.4	10.32	696.8	9.02	765209
R1223O	1.02816	0.01659	0.1193	0.00172	0.893516	99	726.6	9.9	718	8.31	699602
R1224	1.01453	0.01767	0.11824	0.00184	0.893474	101	720.4	10.59	711.2	8.9	1462325
R1225	0.94908	0.01638	0.11318	0.00176	0.901015	102	691.2	10.16	677.6	8.53	2684065
R1226	0.86444	0.01525	0.10482	0.00163	0.881472	102	642.6	9.51	632.5	8.31	1529395
R1227	1.10616	0.02241	0.11908	0.00191	0.791718	96	725.3	11.01	756.3	10.8	1129385
R1227O	0.95913	0.0145	0.1149	0.00164	0.944133	97	701.1	9.49	682.8	7.51	2336937
R1228	3.08687	0.05699	0.23871	0.00371	0.841827	92	1380	19.33	1429.4	14.16	1075704
R1229	0.85115	0.01524	0.10243	0.00159	0.866944	101	628.6	9.31	625.3	8.36	1544700
R1230	0.96649	0.01725	0.11552	0.00179	0.868169	103	704.7	10.37	686.7	8.91	1789891
R1231	3.50136	0.06164	0.26406	0.00409	0.879822	97	1510.6	20.87	1527.5	13.9	1842114
R1231D	0.81429	0.01233	0.09917	0.00143	0.952296	99	609.6	8.37	604.9	6.9	1173842
R1232	2.42692	0.06387	0.20219	0.00351	0.659638	87	1187.1	18.79	1250.6	18.92	808134
R1232D	0.89164	0.01524	0.10648	0.00155	0.851664	99	652.2	9.03	647.3	8.18	1435921

LOWER ADELADIAN: STRUCTURE AND METAMORPHISM

R1233	0.97691	0.01812	0.1128	0.00176	0.841201	100	689	10.2	692	9.31	942560
R1233O	0.99438	0.01538	0.11674	0.00167	0.924896	98	711.8	9.65	701	7.83	996541
R1234	1.03771	0.02696	0.11964	0.00205	0.659529	101	728.5	11.79	722.8	13.43	1104428
R1234D	0.88944	0.01416	0.1068	0.00154	0.905739	99	654.1	8.96	646.1	7.61	355859
R1234W	2.47351	0.04068	0.20069	0.0029	0.878628	107	1179	15.58	1264.3	11.89	712731
R1235	0.99245	0.01818	0.11417	0.00177	0.846323	100	696.9	10.27	700	9.27	1843718

R-12: Filtered Concordia data

Analysis_#	Pb207/U235		Pb206/U238		rho	Concordancy	Pb206/U238	error	Pb207/U235	error	U238
R1231D	0.81429	0.01233	0.09917	0.00143	0.952296	99.22900262	609.6	8.37	604.9	6.9	993318
R1214	0.81542	0.01357	0.10022	0.00155	0.929349	98.34334903	615.7	9.11	605.5	7.59	2828529
R1229	0.85115	0.01524	0.10243	0.00159	0.866944	99.47502386	628.6	9.31	625.3	8.36	1544700
R1215	0.87184	0.01452	0.10463	0.00163	0.935409	99.23616524	641.5	9.49	636.6	7.87	2314894
R1219	0.87836	0.01496	0.10496	0.00163	0.911811	99.48709978	643.4	9.52	640.1	8.09	1732719
R1210	0.89429	0.01457	0.10547	0.00164	0.954407	100.3558168	646.4	9.57	648.7	7.81	3066411
R1221W	0.88532	0.01787	0.10577	0.0016	0.749434	99.35195186	648.1	9.32	643.9	9.62	355859
R1216D	0.88086	0.01299	0.10612	0.00151	0.964889	98.64657029	650.2	8.79	641.4	7.01	811744
R1209D	0.88122	0.01324	0.10614	0.00151	0.946878	98.66215593	650.3	8.81	641.6	7.15	828483
R1232D	0.89164	0.01524	0.10648	0.00155	0.851664	99.24869672	652.2	9.03	647.3	8.18	1007037
R1221D	0.88783	0.01331	0.10668	0.00152	0.950413	98.74502602	653.4	8.87	645.2	7.16	1137944
R1234D	0.88944	0.01416	0.1068	0.00154	0.905739	98.77694542	654.1	8.96	646.1	7.61	1173842
R1206	0.95714	0.01618	0.11098	0.00173	0.922143	100.486367	678.5	10.06	681.8	8.39	979394
R1203	0.97881	0.01668	0.11105	0.00174	0.91946	102.0768891	678.9	10.09	693	8.56	1207555
R1218D	0.93196	0.01403	0.11191	0.0016	0.949709	97.79175197	683.8	9.25	668.7	7.37	980534
R1213D	0.96447	0.01434	0.11259	0.0016	0.955784	99.68013958	687.8	9.3	685.6	7.41	996541
R1225	0.94908	0.01638	0.11318	0.00176	0.901015	98.03240741	691.2	10.16	677.6	8.53	2684065

R1223	0.98618	0.01764	0.11409	0.00178	0.872228	100.0574383	696.4	10.32	696.8	9.02	765209
R1235	0.99245	0.01818	0.11417	0.00177	0.846323	100.4448271	696.9	10.27	700	9.27	1843718
R1222	0.9826	0.01673	0.11505	0.00178	0.908687	98.98860399	702	10.32	694.9	8.57	2522630
R1212	0.98342	0.01693	0.11535	0.00181	0.911471	98.80647911	703.8	10.46	695.4	8.67	2042071
R1230	0.96649	0.01725	0.11552	0.00179	0.868169	97.44572158	704.7	10.37	686.7	8.91	1789891
R1221	0.96873	0.01655	0.1156	0.0018	0.911422	97.53261486	705.2	10.37	687.8	8.54	1854274
R1211	0.97936	0.01604	0.11563	0.0018	0.950473	98.28466119	705.4	10.37	693.3	8.23	2862464
R1207	1.00218	0.01618	0.11593	0.00181	0.967052	99.68887003	707.1	10.43	704.9	8.21	3073145
R1233O	0.99438	0.01538	0.11674	0.00167	0.924896	98.48271987	711.8	9.65	701	7.83	1099281
R1208	1.01755	0.01655	0.11778	0.00183	0.955295	99.28949568	717.8	10.58	712.7	8.33	2371692
R1218	0.99398	0.01753	0.11814	0.00185	0.887913	97.34648513	719.8	10.66	700.7	8.93	705546
R1220	1.02529	0.01735	0.11815	0.00183	0.915302	99.541603	719.9	10.57	716.6	8.7	2169556
R1224	1.01453	0.01767	0.11824	0.00184	0.893474	98.7229317	720.4	10.59	711.2	8.9	1462325
R1227	1.10616	0.02241	0.11908	0.00191	0.791718	104.2740935	725.3	11.01	756.3	10.8	1129385
R1223O	1.02816	0.01659	0.1193	0.00172	0.893516	98.81640517	726.6	9.9	718	8.31	367587
R1210W	1.03735	0.01558	0.1209	0.00172	0.94724	98.20603425	735.8	9.92	722.6	7.77	699602
R1202	1.12743	0.01842	0.12635	0.00198	0.959157	99.93481095	767	11.33	766.5	8.79	1367374
R1234W	2.47351	0.04068	0.20069	0.0029	0.878628	107.2349449	1179	15.58	1264.3	11.89	313589
R1232	2.42692	0.06387	0.20219	0.00351	0.659638	105.3491702	1187.1	18.79	1250.6	18.92	808134
R1228	3.08687	0.05699	0.23871	0.00371	0.841827	103.5797101	1380	19.33	1429.4	14.16	1075704
R1231	3.50136	0.06164	0.26406	0.00409	0.879822	101.1187608	1510.6	20.87	1527.5	13.9	1842114
R1213	3.59638	0.05827	0.26823	0.00416	0.957208	101.1032772	1531.8	21.16	1548.7	12.87	2489799
R1204	4.80103	0.07643	0.31586	0.00493	0.980444	100.881605	1769.5	24.14	1785.1	13.38	1344785

LOWER ADELADIAN: STRUCTURE AND METAMORPHISM

R-12 Concordia Plot All ages.
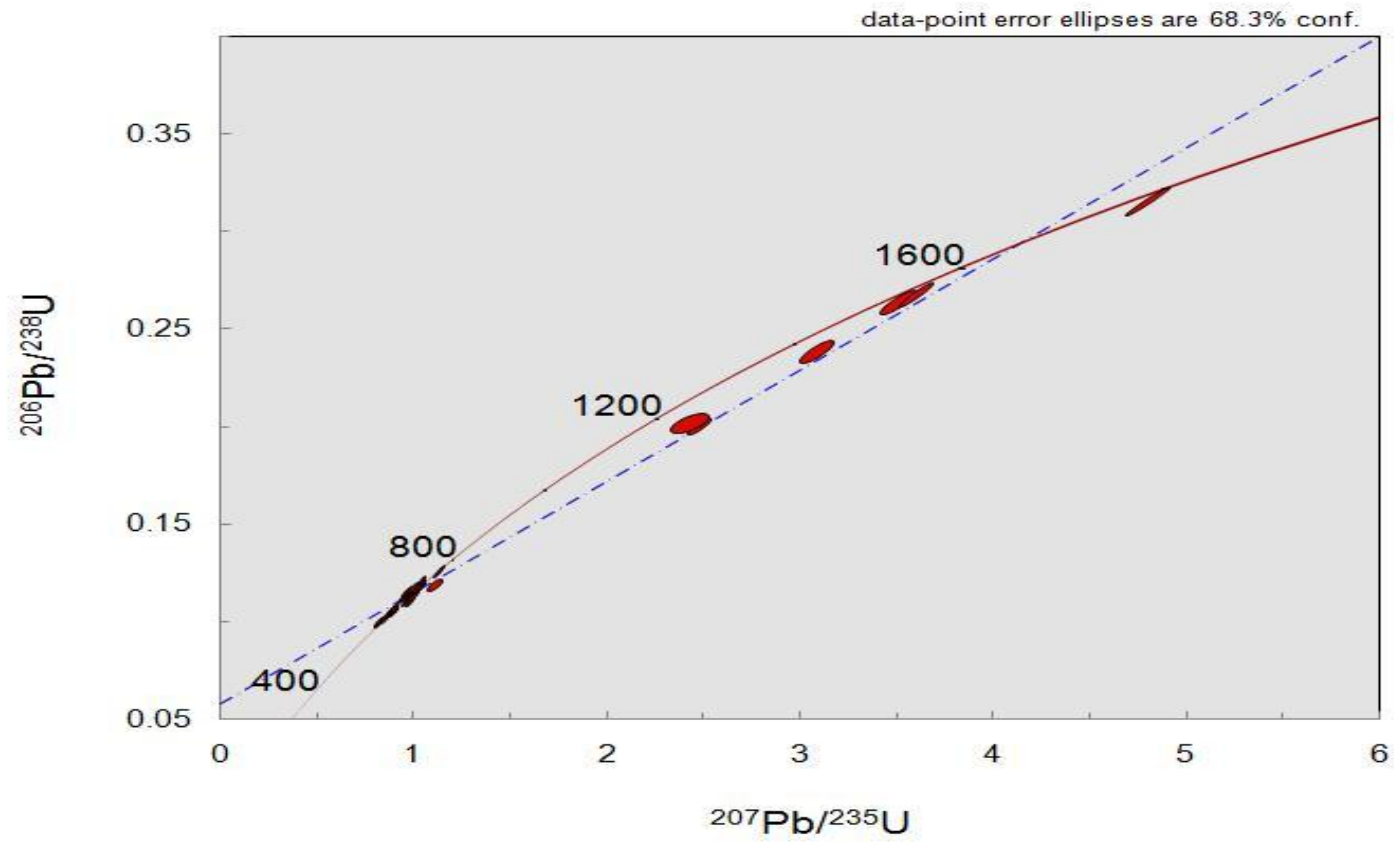
APPENDIX C: R-15 LA-ICP-MS DATA

R-15: Raw Concordia Data

Analysis_#	Pb207/U235		Pb206/U238		rho	Concordancy	Pb206/U238	error	Pb207/U235	error	U238
R15120	0.62278	0.01194	0.07919	0.00137	0.902361	100	491.3	8.2	491.6	7.47	2857082
R1508	0.66795	0.01242	0.08109	0.00137	0.908606	85	502.6	8.19	519.5	7.56	932272
R15122	0.63215	0.01157	0.07661	0.00129	0.920007	79	475.9	7.7	497.4	7.2	1984368
R1504	0.60595	0.01036	0.07335	0.00124	0.988778	76	456.3	7.46	481	6.55	3284684
R1519	0.72415	0.01273	0.08591	0.00145	0.960118	82	531.3	8.6	553.1	7.5	1885704
R15136	0.87696	0.01621	0.10379	0.00174	0.906965	98	636.6	10.17	639.3	8.77	1071065
R15125	0.6861	0.01212	0.08115	0.00136	0.948714	77	503	8.13	530.5	7.3	2227224
R15132	0.76288	0.01363	0.09006	0.00151	0.938438	85	555.9	8.91	575.7	7.85	2403462
R1509	0.79601	0.01368	0.09372	0.00159	0.987182	87	577.5	9.36	594.6	7.74	2425170
R1510	0.75422	0.0131	0.08844	0.00149	0.969983	82	546.3	8.83	570.7	7.58	1858705
R15130	0.8084	0.01456	0.09477	0.00159	0.931518	87	583.7	9.36	601.6	8.18	1548590
R15135	0.70965	0.01436	0.08277	0.00141	0.841852	75	512.6	8.42	544.5	8.53	1735968
R15134	0.8323	0.01544	0.09692	0.00163	0.906581	87	596.4	9.57	614.9	8.56	1269184
R15123	0.83873	0.01502	0.09748	0.00164	0.939465	87	599.6	9.62	618.4	8.29	1315881
R151340	0.88619	0.0166	0.10296	0.00173	0.897008	92	631.7	10.1	644.3	8.94	945147
R1501	0.86827	0.01488	0.10008	0.00171	0.997013	87	614.9	10	634.6	8.09	2115737
R15137	0.84509	0.01566	0.09716	0.00163	0.905339	84	597.8	9.57	622	8.62	1767216
R151342	1.01744	0.01879	0.11697	0.00196	0.907327	100	713.1	11.31	712.6	9.46	792162
R15126	1.03544	0.01897	0.11897	0.00201	0.922181	102	724.7	11.59	721.6	9.46	801923
R1516	0.90562	0.01603	0.10382	0.00175	0.952291	89	636.8	10.23	654.7	8.54	1171742
R15138	1.00123	0.01925	0.11474	0.00193	0.874874	97	700.2	11.19	704.4	9.77	579178
R15131	0.83156	0.01487	0.09475	0.00158	0.932525	80	583.6	9.33	614.5	8.24	2130476

LOWER ADELADIAN: STRUCTURE AND METAMORPHISM

R15128	0.98525	0.01841	0.11208	0.0019	0.907232	93	684.8	11.03	696.3	9.41	536396
R15139	1.09445	0.02372	0.12283	0.00212	0.796366	98	746.8	12.18	750.7	11.5	172916
R1515	0.83171	0.01488	0.09324	0.00157	0.941166	75	574.7	9.23	614.6	8.25	1662430
R1511	1.01899	0.01826	0.11325	0.00193	0.951017	88	691.6	11.17	713.4	9.18	730530
R15133	1.00257	0.01927	0.11091	0.00188	0.881902	85	678	10.89	705.1	9.77	666251
R1513	1.00028	0.01988	0.10766	0.00186	0.869288	77	659.2	10.8	703.9	10.09	607280
R1502	0.98513	0.01679	0.10557	0.00179	0.994845	75	647	10.43	696.2	8.59	2483725
R1514	1.13241	0.02075	0.11948	0.00203	0.927228	82	727.6	11.68	768.9	9.88	535623
R15121	1.11343	0.01993	0.1157	0.00194	0.936751	76	705.8	11.23	759.8	9.58	1046840
R15127	1.27694	0.02369	0.12533	0.00213	0.916073	73	761.2	12.21	835.5	10.56	401153
R151343	1.44254	0.02887	0.13789	0.00235	0.851562	76	832.7	13.29	906.8	12	319970
R1503	1.48833	0.02647	0.13555	0.00232	0.962352	69	819.5	13.16	925.6	10.8	1683224
R15129	1.41984	0.0362	0.12857	0.00238	0.726053	65	779.7	13.58	897.3	15.19	252486
R1517	1.67631	0.02951	0.14703	0.0025	0.965871	70	884.3	14.04	999.6	11.2	639960
R1506	1.91521	0.03534	0.16303	0.00283	0.940738	74	973.6	15.66	1086.4	12.31	2128334
R1505	3.31501	0.05645	0.25976	0.00437	0.987939	101	1488.6	22.34	1484.6	13.28	782427
R1507	2.93176	0.05226	0.22207	0.00377	0.95238	84	1292.8	19.9	1390.1	13.5	600907
R1512	2.74869	0.0476	0.2081	0.00354	0.982313	79	1218.7	18.89	1341.7	12.89	1565280
R1518	3.72793	0.08121	0.27293	0.00493	0.82919	97	1555.7	24.96	1577.4	17.44	39845
R1505D	1.20985	0.01794	0.13358	0.00186	0.939032	100	808.2	10.58	805.1	8.24	1001203
R1506D	0.87385	0.01377	0.1037	0.00146	0.893464	100	636	8.55	637.7	7.46	1076161
R1507D	0.89404	0.01371	0.10717	0.0015	0.91272	99	656.3	8.75	648.5	7.35	2872300
R1508D	2.6817	0.08644	0.20166	0.00386	0.593831	112	1184.2	20.71	1323.4	23.84	34015
R1510W	1.21365	0.01907	0.13183	0.00185	0.8931	101	798.3	10.56	806.9	8.75	486911
R1511W	0.95863	0.01547	0.11367	0.0016	0.872238	98	694	9.28	682.6	8.02	973330
R1512D	0.86214	0.01287	0.10376	0.00144	0.929676	99	636.4	8.41	631.3	7.02	2541333
R1513D	1.12493	0.01668	0.12823	0.00178	0.936181	98	777.8	10.17	765.3	7.97	2018910

R1516W	2.61239	0.0391	0.20523	0.00286	0.931079	108	1203.4	15.28	1304.1	10.99	753069
R1517D	0.90042	0.01345	0.10853	0.00151	0.93143	98	664.2	8.76	652	7.19	2122588
R1523D	1.0704	0.01664	0.12193	0.0017	0.896873	100	741.7	9.79	738.9	8.16	1492888
R1525D	0.97091	0.01474	0.11501	0.0016	0.916359	98	701.8	9.24	688.9	7.6	1367683
R1526W	0.94986	0.01602	0.10655	0.00151	0.840273	104	652.7	8.79	678	8.34	591398
R1527D	0.90304	0.01355	0.10787	0.00149	0.920563	99	660.4	8.69	653.4	7.23	2658054
R1528D	0.86863	0.01306	0.10438	0.00145	0.923937	99	640	8.44	634.8	7.1	2934071
R1529L	1.0154	0.0154	0.11619	0.00161	0.913637	100	708.6	9.32	711.6	7.76	929925
R1530W	1.39791	0.02308	0.11921	0.00168	0.853572	122	726	9.7	888	9.77	511961
R1531O	1.04282	0.01579	0.1138	0.00158	0.916942	104	694.8	9.16	725.3	7.85	630125
R1533D	0.97402	0.01429	0.11473	0.00159	0.944617	99	700.1	9.17	690.5	7.35	1811442
R1534D	0.80851	0.01193	0.09695	0.00134	0.936703	101	596.5	7.89	601.6	6.7	1425553
R1535D	0.91126	0.01392	0.10786	0.00149	0.904334	100	660.3	8.7	657.7	7.4	1499828
R1536D	0.82328	0.01416	0.09757	0.00137	0.816373	102	600.2	8.03	609.9	7.89	2316684
R1536W	0.9746	0.01487	0.11625	0.00161	0.907713	97	709	9.3	690.8	7.65	1156440
R1537D	1.02171	0.01533	0.11819	0.00163	0.919163	99	720.1	9.41	714.8	7.7	1386591
R1537W	1.07625	0.01701	0.12311	0.00171	0.878844	99	748.5	9.83	741.8	8.32	567904
R1538D	0.64482	0.01068	0.08344	0.00116	0.839365	98	516.6	6.92	505.3	6.6	2759764
R1539D	0.88907	0.01365	0.10528	0.00146	0.903255	100	645.3	8.51	645.9	7.34	788882

R-15: Filtered Concordia Data

Analysis_#	Pb207/U235		Pb206/U238		rho	Concordancy	Pb206/U238		Pb207/U235		U238
R15120	0.62278	0.01194	0.07919	0.00137	0.91272	82.38486587	491.3	8.2	491.6	7.47	2857082
R1519	0.72415	0.01273	0.08591	0.00145	0.893464	96.78964723	531.3	8.6	553.1	7.5	1885704
R15134	0.8323	0.01544	0.09692	0.00163	0.872238	85.4442344	596.4	9.57	614.9	8.56	1269184
R1501	0.86827	0.01488	0.10008	0.00171	0.952291	114.6069869	614.9	10	634.6	8.09	2115737
R1506D	0.87385	0.01377	0.1037	0.00146	0.893464	98.68114818	636	8.55	637.7	7.46	1076161
R1512D	0.86214	0.01287	0.10376	0.00144	0.929676	103.5807292	636.4	8.41	631.3	7.02	2541333
R1516	0.90562	0.01603	0.10382	0.00175	0.907327	75.11436414	636.8	10.23	654.7	8.54	1171742
R1528D	0.86863	0.01306	0.10438	0.00145	0.923937	103.4928849	640	8.44	634.8	7.1	2934071
R1507D	0.89404	0.01371	0.10717	0.0015	0.91272	105.2268719	656.3	8.75	648.5	7.35	2872300
R1513	1.00028	0.01988	0.10766	0.00186	0.874874	78.89047126	659.2	10.8	703.9	10.09	607280
R1535D	0.91126	0.01392	0.10786	0.00149	0.904334	101.366288	660.3	8.7	657.7	7.4	1499828
R1517D	0.90042	0.01345	0.10853	0.00151	0.93143	108.5826385	664.2	8.76	652	7.19	2122588
R15128	0.98525	0.01841	0.11208	0.0019	0.593831	73.2345584	684.8	11.03	696.3	9.41	536396
R1511	1.01899	0.01826	0.11325	0.00193	0.907232	81.549485	691.6	11.17	713.4	9.18	730530
R1511W	0.95863	0.01547	0.11367	0.0016	0.872238	107.2477206	694	9.28	682.6	8.02	973330
R1533D	0.97402	0.01429	0.11473	0.00159	0.944617	105.8992588	700.1	9.17	690.5	7.35	1811442
R15138	1.00123	0.01925	0.11474	0.00193	0.929676	83.94888358	700.2	11.19	704.4	9.77	579178
R1529L	1.0154	0.0154	0.11619	0.00161	0.913637	98.00829876	708.6	9.32	711.6	7.76	929925
R151342	1.01744	0.01879	0.11697	0.00196	0.931079	91.53745834	713.1	11.31	712.6	9.46	792162
R1537D	1.02171	0.01533	0.11819	0.00163	0.919163	102.9155352	720.1	9.41	714.8	7.7	1386591
R1514	1.13241	0.02075	0.11948	0.00203	0.796366	77.49823654	727.6	11.68	768.9	9.88	535623
R1523D	1.0704	0.01664	0.12193	0.0017	0.896873	101.2836269	741.7	9.79	738.9	8.16	1492888
R15139	1.09445	0.02372	0.12283	0.00212	0.936181	97.37171464	746.8	12.18	750.7	11.5	172916

LOWER ADELADIAN: STRUCTURE AND METAMORPHISM

R1513D	1.12493	0.01668	0.12823	0.00178	0.936181	106.4021888	777.8	10.17	765.3	7.97	2018910
R1505D	1.20985	0.01794	0.13358	0.00186	0.93143	101.3162843	808.2	10.58	805.1	8.24	1001203
R1506	1.91521	0.03534	0.16303	0.00283	0.960118	100.6082725	973.6	15.66	1086.4	12.31	2128334
R1508D	2.6817	0.08644	0.20166	0.00386	0.593831	75.96869387	1184.2	20.71	1323.4	23.84	34015
R1516W	2.61239	0.0391	0.20523	0.00286	0.931079	81.57537961	1203.4	15.28	1304.1	10.99	753069
R1512	2.74869	0.0476	0.2081	0.00354	0.906581	88.25931598	1218.7	18.89	1341.7	12.89	1565280
R1507	2.93176	0.05226	0.22207	0.00377	0.902361	73.71848262	1292.8	19.9	1390.1	13.5	600907
R1505	3.31501	0.05645	0.25976	0.00437	0.82919	75.8225324	1488.6	22.34	1484.6	13.28	782427
R1518	3.72793	0.08121	0.27293	0.00493	0.939032	70.0324701	1555.7	24.96	1577.4	17.44	39845

R-15: Concordia Plot All Ages